

Electrokinetic energy conversion of two-layer fluids through nanofluidic channels

Zhaodong Ding¹, Yongjun Jian^{1,†} and Wenchang Tan²

¹School of Mathematical Science, Inner Mongolia University, Hohhot, Inner Mongolia 010021, PR China

²State Key Laboratory for Turbulence and Complex Systems, and Department of Mechanics and Engineering Science, College of Engineering, Peking University, Beijing 100871, PR China

(Received 28 December 2017; revised 4 December 2018; accepted 3 January 2019;
first published online 29 January 2019)

Based on the Onsager reciprocal relation in the linear response regime, we first clarify the equivalence of thermodynamic and electric circuit analyses for electrokinetic energy conversion. Then we present a streaming-potential-based nanofluidic energy conversion system which comprises two immiscible fluids that form a flat interface in a slit-like channel. The validity of the Onsager reciprocal relation to such a two-fluid system is verified. The performance of such an energy converter is illustrated by considering two concrete oil–water systems with different properties. In both cases, we predict that the binary system with a thin oil layer increases both the maximum output power and the energy conversion efficiency, and this enhancement depends strongly on the mobile charges present at the oil–water interface, the salt concentration and the interface location. Concretely, for negatively charged interfaces, we find that the optimal efficiency increases with the interfacial charge for relatively thin oil layers; while for relatively thick oil layers, the interfacial charge has the opposite effect (i.e. reduction effect) on the energy conversion efficiency in the ranges of the parameters. We further investigate these systems from the viewpoint of energy transfer by deriving the related energy equation. We find that viscous dissipation consumes most of the power (more than 90%), in both single-phase and two-fluid flows. However, the ratio of the viscous dissipation to the power input decreases with increase of the interfacial charge density for the case of a relatively thin oil layer in two-fluid flows. Meanwhile, although the presence of interfacial charges can lead to an increase in electrical dissipation, the amount of the increased power consumption is less than that of the reduced viscous dissipation in the case of a thin oil layer. Therefore, for two-fluid energy converters, the total power consumption can be reduced and the efficiency is improved.

Key words: microfluidics

1. Introduction

In recent decades, electrokinetic phenomena, such as electro-osmosis, streaming potential and streaming current, have attracted wide attention and application thanks to advances in micro- and nanofabrication technologies (Schoch, Han & Renaud 2008;

† Email address for correspondence: jjanyj@imu.edu.cn

Sparreboom, van den Berg & Eijkel 2010). In general, most solid surfaces obtain a surface electrical charge when they are in contact with a polarizable electrolyte solution. This surface charge leads to the formation of an electrical double layer (EDL) at the solid–liquid interface (Li 2004; Masliyah & Bhattacharjee 2006). The charged walls of a microchannel will become increasingly important in the nano-regime because of the larger surface-to-volume ratio (Stein, Kruithof & Dekker 2004; Bocquet & Charlaix 2010). When pressure-driven transport ensues in a microchannel, the fluid flow drives the net charge within the EDL downstream, thereby resulting in an electric current, known as the streaming current. The accumulation of charges at the channel downstream creates an electric potential difference between the two ends of the channel, termed the streaming potential (Das, Guha & Mitra 2013). The establishment of streaming current and streaming potential in microchannels provides the possibility of converting mechanical energy into electrical power, as reported by experimental and theoretical studies (Osterle 1964; Yang *et al.* 2003; Olthuis *et al.* 2005; Daiguji *et al.* 2006; Xuan & Li 2006; Xie *et al.* 2008; Chang & Yang 2010, 2011; Wang & Kang 2010; Zhang *et al.* 2015). Especially, nanoscale fluidic devices allow the probing of the regime of EDL overlap, where the electrokinetic energy conversion efficiency is expected to be highest (Daiguji *et al.* 2004*b*; van der Heyden *et al.* 2006, 2007; Pennathur, Eijkel & van den Berg 2007; Siria *et al.* 2013; Ding *et al.* 2017).

For practical micro- or nanochannels filled with electrolyte solution, it is found that the electrical conductance of the Stern layer within the EDL reduces the efficiency and power output significantly (van der Heyden *et al.* 2007; Davidson & Xuan 2008*a*). On the other hand, recent studies have shown that the energy conversion efficiency may be improved remarkably by employing, for example, velocity slip (Davidson & Xuan 2008*b*; Ren & Stein 2008), soft nanochannels (Chanda, Sinha & Das 2014; Patwary, Chen & Das 2016), steric effect (Bandopadhyay & Chakraborty 2011), viscoelastic fluids (Bandopadhyay & Chakraborty 2012; Jian *et al.* 2017), time-periodic pressure (Goswami & Chakraborty 2010), polymer addition (Nguyen *et al.* 2013), buffer anions effect (Mei, Yeh & Qian 2017), transverse magnetic fields (Munshi & Chakraborty 2009) and layering of large ions near the wall–liquid interface (Gillespie 2012). Liu *et al.* (2016) presented a flexible microfluidics nanogenerator, which may offer an approach for building up self-powered systems by harvesting human mechanical energy. However, there exist two different approaches to evaluate efficiency in the literature. Some groups (e.g. Daiguji *et al.* 2006; Xuan & Li 2006; Davidson & Xuan 2008*b*; Chang & Yang 2010) computed the output power and conversion efficiency based on thermodynamic analysis; while other groups (e.g. Yang *et al.* 2003; van der Heyden *et al.* 2006, 2007; Gillespie 2012) used electric circuit analysis. We will review and discuss them in the next section.

Recently, Xie *et al.* (2011) showed that injection of gas bubbles into a liquid-filled channel increases both the maximum output power and the energy conversion efficiency. In subsequent work (Sherwood *et al.* 2013), they presented a theoretical analysis of the generation of streaming currents and electrical power by two-phase flow under various flow patterns in a rectangular microchannel where low wall zeta potential and thin EDL relative to the channel height have been assumed. In their research, the injection of a second, non-conducting fluid phase tends to decrease the effective cross-section of the channel, thereby decreasing the conduction current, which causes power dissipation and lowers efficiency. However, this mechanism may be invalid in nanochannels with a thick EDL because the reduction in effective cross-section also leads to a decrease in streaming current.

In nanofluidic channels, the electrostatic properties at the liquid–liquid interface may have a significant effect on electrokinetic energy conversion. In this paper, we focus on the performance of nanofluidic energy conversion systems using a model of two-layer fluid flow where the effects of electrostatic properties at the liquid–liquid interface are investigated in detail. On the other hand, in order to examine the energy transfer among different forms in electrokinetic flows, we derive the mechanical energy equation by combining thermodynamic and fluid mechanics on the system.

In a two-layer fluid system consisting of two immiscible electrolytes, an EDL is also formed at the liquid–liquid interface (Choi *et al.* 2011; Gopmandal & Ohshima 2017; Saha, Gopmandal & Ohshima 2017). However, a key difference is the presence of mobile ions along the liquid–liquid interface (Lee & Li 2006; Movahed *et al.* 2012). In addition, Volkov *et al.* (1996) have pointed out that, at the interface of two immiscible electrolyte solutions, a narrow region exists where the electric potential changes abruptly due to the adsorption of ions. The sharp change at this layer can often be described by a zeta potential jump across the interface (Choi *et al.* 2011; Su *et al.* 2013; Jian *et al.* 2014; Shit *et al.* 2016). Therefore, for practical purposes, the surface charge and zeta potential jump are incorporated to describe the boundary condition at the interface. Furthermore, semi-analytical expressions for the velocity, output power and energy transfer efficiency for the two-fluid system are obtained by considering large wall potentials, and the finite conductance of the Stern layer.

This paper is organized as follows. In §2 we review the general framework for electrokinetic energy conversion in micro- and nanofluidic channels. The physical description of a two-fluid system and the solution to the equations governing the distributions of EDL potential and velocity in two-layer fluids are presented in §3. We examine in §4 the performance of practical electrokinetic energy converters. A summary of our results is provided in §5.

2. General framework for electrokinetic energy conversion

As stated in the introduction, when the flow is driven by a pressure gradient, a streaming current and streaming potential can be established and pressure-to-voltage energy conversion can be achieved. Within the linear response regime of electrokinetic flows, the electric current and flow rate through a micro/nanochannel are often described well by the Onsager reciprocal relation (Brunet & Ajdari 2004; van der Heyden *et al.* 2006; Xuan & Li 2006)

$$Q = L_{11}(-\Delta p) + L_{12}(-\Delta\phi), \quad (2.1)$$

$$I = L_{21}(-\Delta p) + L_{22}(-\Delta\phi), \quad (2.2)$$

where L_{11} represents the hydrodynamic conductance of the channel, $L_{12} = L_{21}$ characterizes the streaming conductance, L_{22} indicates the electrical conductance of the channel, and Δp and $\Delta\phi$ are the pressure difference and the electric potential difference between the channel ends, respectively. The conductance tensor $\mathbf{L} = (L_{ij})$ must be positive definite by the second law of thermodynamics (Prigogine 1968). In (2.2), the term $L_{21}(-\Delta p)$ is the so-called streaming current (denoted by I_s), while $L_{22}(-\Delta\phi)$ is the conduction current (I_c). Furthermore, the zero-current condition (i.e. $I = 0$) leads to an open-circuit voltage, namely, the streaming potential $\Delta\phi_s = L_{21}(-\Delta p)/L_{22}$. It should be noted that the linear Onsager reciprocal relation will fail when the non-equilibrium concentration polarization phenomenon occurs at the two ends of a channel (Chang & Yang 2010, 2011).

In the literature, the electrokinetic energy conversion efficiency has been calculated in different ways. For example, Xuan & Li (2006) calculate the maximum conversion efficiency based on thermodynamics while the work of van der Heyden *et al.* (2006) is based on the equivalent circuit. We compare these two ways in the following.

2.1. Thermodynamic analysis

The generation power W and conversion efficiency ξ can be written as

$$W = I\Delta\phi \quad \text{and} \quad \xi = \frac{I\Delta\phi}{Q(-\Delta p)}. \quad (2.3a,b)$$

The generation power is maximized by $\Delta\phi = -\Delta p L_{12}/2L_{22}$, which is exactly half of the streaming potential. The maximum generation power and the corresponding conversion efficiency are given by (Xuan & Li 2006)

$$W_{max W} = \frac{I_s \Delta\phi_s}{4} = \frac{\alpha}{4} L_{11} (\Delta p)^2 \quad \text{and} \quad \xi_{max W} = \frac{I_s \Delta\phi_s}{4Q(-\Delta p)} = \frac{\alpha}{2(2-\alpha)}, \quad (2.4a,b)$$

where the subscript $max W$ indicates the condition of maximum generation power, $\alpha = L_{12}L_{21}/L_{11}L_{22}$ is the figure of merit for electrokinetic energy conversion, and $0 \leq \alpha < 1$ due to the positive definiteness of \mathbf{L} . On the other hand, when the voltage satisfies $\Delta\phi = -\Delta p(1 - \sqrt{1-\alpha})L_{11}/L_{12}$, the conversion efficiency is maximized. At this condition, the generation power and efficiency are given by (Xuan & Li 2006)

$$W_{max \xi} = L_{11} \frac{\sqrt{1-\alpha}(1 - \sqrt{1-\alpha})^2}{\alpha} (\Delta p)^2 \quad \text{and} \quad \xi_{max \xi} = \frac{(1 - \sqrt{1-\alpha})^2}{\alpha}, \quad (2.5a,b)$$

where the subscript max indicates the condition of maximum generation efficiency.

2.2. Electric circuit analysis

Consider such a fluidic device connected to an electrical resistor (with resistance R_L) in a circuit (see figure 1*b*). The efficiency is defined as the electrical power, $\Delta\phi^2/R_L$, consumed by the load divided by the input mechanical pumping power, $Q(-\Delta p)$. It is convenient to define a rescaled load resistance, $\Omega = R_L/R_{ch}$, relative to the channel resistance, $R_{ch} = 1/L_{22}$. The maximum electrical power can be achieved at $\Omega = 1$. At this condition, the maximum power and the corresponding conversion efficiency are the same as in (2.4). Furthermore, the optimal efficiency and the corresponding generation power are found to be

$$W_{max \xi} = L_{11} \frac{\sqrt{1-\alpha}(1 - \sqrt{1-\alpha})^2}{\alpha} (\Delta p)^2 \quad \text{and} \quad \xi_{max \xi} = \frac{\alpha}{\alpha + 2(\sqrt{1-\alpha} + 1 - \alpha)}, \quad (2.6a,b)$$

for $\Omega = 1/\sqrt{1-\alpha}$ (van der Heyden *et al.* 2006). It is easy to verify that the efficiencies in (2.5) and (2.6) are the same, although they are in different forms.

Interestingly, we find that the results (i.e. the electrical power and efficiency) under the conditions of maximum output power and/or maximum efficiency are the same whether based on thermodynamic or electric circuit analyses. Table 1 summarizes the electrical powers and conversion efficiencies obtained in different ways.

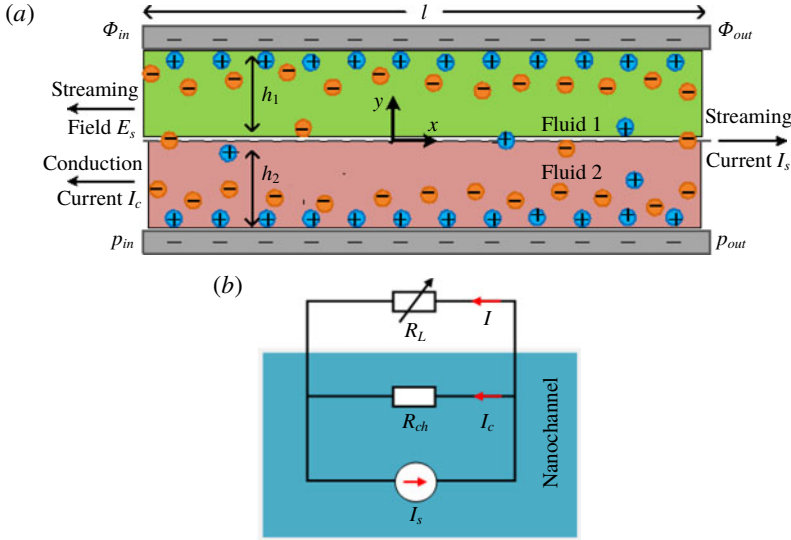


FIGURE 1. (Colour online) (a) Schematic illustration of electrokinetic energy conversion in a nanochannel filled with two-layer fluids. A positive external pressure gradient $-\Delta p/l = -(p_{out} - p_{in})/l$ is applied across the nanochannel in the x -direction, which drives the flow of mobile ions and thus induces a streaming current I_s and a streaming electric field of strength $E_s = -\Delta\phi/l = -(\Phi_{out} - \Phi_{in})/l$. This electric field, in turn, generates a current (conduction current I_c) to flow back against the direction of the pressure-driven flow. (b) Equivalent electric circuit of the considered system connected to an external load resistor with adjustable resistance R_L .

Methods	Power ^a	Efficiency ^a	Power ^b	Efficiency ^b
Thermodynamic	$\frac{\alpha}{4}L_{11}(\Delta p)^2$	$\frac{\alpha}{2(2-\alpha)}$	$L_{11}\frac{\sqrt{1-\alpha}(1-\sqrt{1-\alpha})^2}{\alpha}(\Delta p)^2$	$\frac{(1-\sqrt{1-\alpha})^2}{\alpha}$
Electric circuit	$\frac{\alpha}{4}L_{11}(\Delta p)^2$	$\frac{\alpha}{2(2-\alpha)}$	$L_{11}\frac{\sqrt{1-\alpha}(1-\sqrt{1-\alpha})^2}{\alpha}(\Delta p)^2$	$\frac{\alpha}{\alpha + 2(\sqrt{1-\alpha} + 1 - \alpha)}$
Approximation	$\frac{\alpha}{4}L_{11}(\Delta p)^2$	$\frac{\alpha}{4}$	$\frac{\alpha}{4}L_{11}(\Delta p)^2$	$\frac{\alpha}{4}$

TABLE 1. Summary of electrical power and conversion efficiency under the maximum power generation and/or maximum conversion efficiency conditions, based on thermodynamic and electric circuit analyses, respectively.

^aIndicates the condition of maximum power generation.

^bIndicates the condition of maximum conversion efficiency, and the approximation is for small α .

Comparing the two generation powers W_{maxW} and $W_{max\xi}$ in (2.4) and (2.5), we find that they are identical up to $O(\alpha^2)$ for small α by means of

$$\frac{\sqrt{1-\alpha}(1-\sqrt{1-\alpha})^2}{\alpha} = \frac{\alpha}{4} - \frac{\alpha^3}{64} + O(\alpha^4). \tag{2.7}$$

Similarly, the two conversion efficiencies ξ_{maxW} and $\xi_{max\xi}$ are identical up to $O(\alpha^2)$ by means of

$$\frac{(1 - \sqrt{1 - \alpha})^2}{\alpha} = \frac{\alpha}{4} + \frac{\alpha^2}{8} + \frac{5\alpha^3}{64} + O(\alpha^4), \quad (2.8)$$

$$\frac{\alpha}{2(2 - \alpha)} = \frac{\alpha}{4} + \frac{\alpha^2}{8} + \frac{\alpha^3}{16} + O(\alpha^4). \quad (2.9)$$

Note that the upper bound of ξ_{maxW} is $1/2$ while the upper bound of $\xi_{max\xi}$ is 1 . However, for typical electrokinetic energy converters, the value of α is small (e.g. $\alpha < 0.5$), so the above two extreme powers (or efficiencies) are essentially close to each other (Xuan & Li 2006).

A few researchers (e.g. Daiguji *et al.* 2004b; Olthuis *et al.* 2005; Berli 2010; Chanda *et al.* 2014) calculated the input volume flow rate Q in the definition of the efficiency ξ as the purely pressure-driven volume flow rate, i.e. $Q = L_{11}(-\Delta p)$. In this situation, the maximum efficiency that can be achieved is

$$\xi_{max} = \frac{I_s \Delta \phi_s}{4L_{11}(\Delta p)^2} = \frac{\alpha}{4}. \quad (2.10)$$

It is easy to see that the efficiency ξ_{max} is the leading term of the above efficiency ξ_{maxW} or $\xi_{max\xi}$ by using (2.8) and (2.9). For small α , these extreme efficiencies achieved under three different conditions are nearly identical, i.e. $\xi_{max} \approx \xi_{maxW} \approx \xi_{max\xi}$.

3. Two-fluid energy converter

We consider a steady unidirectional flow of two immiscible viscous fluids of constant viscosity μ_i , electrical permittivity ε_i and thickness h_i confined between two micro parallel plates at distance h ($= h_1 + h_2$), where $i = 1$ and 2 are associated with the upper (fluid 1) and the lower layer (fluid 2), respectively. The channel walls are considered to bear a negative surface charge. We assume the width w and the length l of the parallel plates are much larger than the height, i.e. $l, w \gg h$, and the interface between these two immiscible fluids is planar. A two-dimensional coordinate system (x, y) is established at the fluid–fluid interface, where the x -axis is tangential to the plate surface and the y -axis is perpendicular to the plate surface, as sketched in figure 1(a). We note that this model makes several simplifying assumptions by focusing entirely on the properties of the slit-like channel. For example, it ignores the entrance effects where the channel meets the reservoirs, and takes the potential drop between the electrode and the electrolyte to be zero.

3.1. Electrical double-layer electric potential distribution

We assume that the fluids contain binary symmetric electrolyte ions with valence $z_+ = -z_- = z$. Owing to the interaction between the electrolyte ions and the charged walls as well as the liquid–liquid interface, EDLs are formed. In addition, in a two-fluid system, an unequal partitioning of micro-ions between the two liquid phases is induced by the difference in the dielectric constant (Ohshima *et al.* 1985; Leunissen *et al.* 2007; Gopmandal & Ohshima 2017; Saha *et al.* 2017). Considering the ion partitioning effect, the Boltzmann distribution satisfied by the electrolyte ions

can be written as

$$\left. \begin{aligned} n_{\pm} &= n_{\infty} \exp\left(\mp \frac{ez\psi}{k_B T}\right), & 0 < y < h_1, \\ n_{\pm} &= b_{\pm} n_{\infty} \exp\left(\mp \frac{ez\psi}{k_B T}\right), & -h_2 < y < 0. \end{aligned} \right\} \quad (3.1)$$

Here, ψ is the EDL electric potential, n_{\pm} are the concentrations of the electrolyte ions, b_{\pm} are the ion partition coefficients of the electrolyte ions with $n_{\pm}(0-) = b_{\pm} n_{\pm}(0+)$, n_{∞} is the bulk ionic concentration at $\psi = 0$, e is the electronic charge, k_B is the Boltzmann constant and T is the absolute temperature.

The equilibrium electric potential ψ relative to the bulk electrolyte and the local volumetric net charge density $\rho_e = ez(n_+ - n_-)$ can be related through the Poisson equation as

$$\nabla^2 \psi = -\frac{\rho_e}{\varepsilon_i}, \quad i = 1, 2. \quad (3.2)$$

For the fully developed flow, the distribution of the electric potential can be regarded as a function of y , i.e. $\psi = \psi(y)$.

To solve the electric potential distributions within fluids 1 and 2, appropriate boundary conditions must be imposed. In previous studies, three different models have been adopted for the electrostatic properties of the surface: constant zeta potential (Yang *et al.* 2003; Davidson & Xuan 2008*a,b*), constant surface charge density (Daiguji, Yang & Majumdar 2004*a*; Daiguji *et al.* 2004*b*; Stein *et al.* 2004; Chang & Yang 2010) and local chemical equilibrium (Behrens & Grier 2001; van der Heyden *et al.* 2007; Wang & Kang 2010). The surface charge essentially varies with the bulk ionic concentration, the pH value and the temperature of the solution, and the double-layer interactions. This implies that the chemical equilibrium model may be the most suitable one to describe the solid–liquid interface, compared with the other two models. But there are many parameters that need to be specified beforehand, such as the surface density Γ of chargeable sites, pH value, equilibrium constant pK describing the dissociation of SiOH groups and Stern layer phenomenological capacity C (Behrens & Grier 2001). In order to avoid excessive complexity, the condition of constant surface charge density is used, which yields reasonable results and is much better than assuming a constant zeta potential (Stein *et al.* 2004; van der Heyden, Stein & Dekker 2005). Furthermore, the surface charges are related to the electric potential $\psi(y)$ through Gauss' law:

$$\sigma_1 = \varepsilon_1 \left. \frac{d\psi}{dy} \right|_{y=h_1} \quad \text{and} \quad \sigma_2 = -\varepsilon_2 \left. \frac{d\psi}{dy} \right|_{y=-h_2}, \quad (3.3a,b)$$

where σ_1 and σ_2 are the surface charge densities of the upper plate and lower plate, respectively.

At the liquid–liquid interface ($y = 0$), we impose the potential difference $\Delta\psi$ and Gauss' law for the electrical displacement (Choi *et al.* 2011; Jian *et al.* 2014):

$$\psi|_{y=0-} - \psi|_{y=0+} = \Delta\psi \quad \text{and} \quad \varepsilon_2 \left. \frac{d\psi}{dy} \right|_{y=0-} - \varepsilon_1 \left. \frac{d\psi}{dy} \right|_{y=0+} = \sigma_s. \quad (3.3c,d)$$

Here σ_s denotes the interface charge density, which implies that the normal component of the electric displacement vector is discontinuous; $\Delta\psi$ and σ_s are considered to be

independent parameters (Choi *et al.* 2011). In addition, the total charges in the channel can be expressed as

$$Q_c = A \left(\int_{-h_2}^{h_1} \rho_e dy + \sigma_1 + \sigma_2 + \sigma_s \right), \quad (3.4)$$

where A is the area of the plate. Substituting (3.3) into (3.4) yields $Q_c = 0$. This verifies the condition of electroneutrality in the channel.

We introduce the following non-dimensional variables:

$$\left. \begin{aligned} [Y, H_1, H_2] &= \frac{1}{h} [y, h_1, h_2], & [\Psi, \Delta\Psi] &= \frac{ze}{k_B T} [\psi, \Delta\psi], \\ [\bar{\sigma}_1, \bar{\sigma}_2, \bar{\sigma}_s] &= \frac{zeh}{\varepsilon_1 k_B T} [\sigma_1, \varepsilon_r^{-1} \sigma_2, \sigma_s], \end{aligned} \right\} \quad (3.5)$$

and $K = h/\lambda_D$ with the Debye screening length $\lambda_D = \sqrt{\varepsilon_1 k_B T / 2n_\infty z^2 e^2}$, where $\varepsilon_r = \varepsilon_2/\varepsilon_1$ denotes the permittivity ratio. With these scaled variables, (3.1) and (3.2) reduce to

$$\frac{d^2\Psi}{dY^2} = \begin{cases} K^2 \sinh \Psi, & 0 < Y < H_1, \\ (2\varepsilon_r)^{-1} K^2 [-b_+ \exp(-\Psi) + b_- \exp \Psi], & -H_2 < Y < 0. \end{cases} \quad (3.6)$$

The corresponding dimensionless boundary conditions become

$$\left. \begin{aligned} \bar{\sigma}_1 &= \frac{d\Psi}{dY} \Big|_{Y=H_1}, & \bar{\sigma}_2 &= -\frac{d\Psi}{dY} \Big|_{Y=-H_2}, & \Psi|_{Y=0^-} - \Psi|_{Y=0^+} &= \Delta\Psi, \\ \varepsilon_r \frac{d\Psi}{dY} \Big|_{Y=0^-} - \frac{d\Psi}{dY} \Big|_{Y=0^+} &= \bar{\sigma}_s. \end{aligned} \right\} \quad (3.7)$$

Equation (3.6) with the boundary conditions (3.7) is solved iteratively through a second-order central difference scheme. The iteration procedure starts with a guessed value of the potential. Here we assume that the partition coefficients for cations and anions are identical, i.e. $b_+ = b_- = b$. The detailed scheme and algorithm can be found in appendix A. Meanwhile, the convergence and validity of the algorithm and the dependence of the results on the number of grid points are also analysed.

3.2. Flow field coupled with electrokinetic interaction

The flow maintained by constant pressure gradient $-dp/dx = -\Delta p/l$ is assumed to be one-dimensional, steady and fully developed; the body force is the electric field force $\rho_e E_s = \rho_e (-\Delta\phi)/l$. Thus in such a two-fluid system the governing equation for the velocity can be described by

$$\mu_i \frac{d^2 u}{dy^2} - \frac{\Delta p}{l} + \rho_e E_s = 0, \quad i = 1, 2, \quad (3.8)$$

where $u(y)$ is the axial velocity along the positive x -direction. At the solid-liquid interface, the no-slip conditions are given by $u|_{y=h_1} = u|_{y=-h_2} = 0$. The continuity of the velocity as well as the balance of the total stresses including the Maxwell stress

and shear stress between the two layers should be applied at the liquid–liquid interface (Jian *et al.* 2014)

$$u|_{y=0^+} = u|_{y=0^-}, \quad \left(\mu_1 \frac{du}{dy} - \varepsilon_1 E_s \frac{d\psi}{dy} \right) \Big|_{y=0^+} = \left(\mu_2 \frac{du}{dy} - \varepsilon_2 E_s \frac{d\psi}{dy} \right) \Big|_{y=0^-}. \quad (3.9a,b)$$

Combining the governing equations in different fluids with the related boundary conditions, the analytical solution of the velocity distribution can be derived as

$$u = \begin{cases} \frac{\Delta p}{2l\mu_1} [y^2 - h_1^2 + A_2(y - h_1)] + \frac{\Delta\phi}{l\mu_1} [A_1(y - h_1) + \varepsilon_1(\psi_{1,w} - \psi)], & 0 \leq y \leq h_1, \\ \frac{\Delta p}{2l\mu_2} [y^2 - h_2^2 + A_2(y + h_2)] + \frac{\Delta\phi}{l\mu_2} [A_1(y + h_2) + \varepsilon_2(\psi_{2,w} - \psi)], & -h_2 \leq y \leq 0, \end{cases} \quad (3.10)$$

where

$$A_1 = \frac{\mu_r \varepsilon_1 (\psi_{1,w} - \psi(0+)) - \varepsilon_2 (\psi_{2,w} - \psi(0-))}{\mu_r h_1 + h_2}, \quad A_2 = \frac{h_2^2 - \mu_r h_1^2}{\mu_r h_1 + h_2}, \quad (3.11a,b)$$

$\mu_r = \mu_2/\mu_1$ denotes the viscosity ratio, and $\psi_{1,w}$ and $\psi_{2,w}$ are the wall zeta potentials of the upper plate and lower plate, respectively.

Integrating the velocity (3.10) over the channel cross-section gives the volumetric flow rate Q and then yields the expressions for the phenomenological coefficients in (2.1) as

$$L_{11} = \frac{w}{2l} \left[\frac{2h_1^3}{3\mu_1} + \frac{2h_2^3}{3\mu_2} + A_2 \left(\frac{h_1^2}{2\mu_1} - \frac{h_2^2}{2\mu_2} \right) \right] \quad (3.12)$$

and

$$L_{12} = \frac{w}{l} \left[\frac{\varepsilon_1}{\mu_1} \int_0^{h_1} (\psi(y) - \psi_{1,w}) dy + \frac{\varepsilon_2}{\mu_2} \int_{-h_2}^0 (\psi(y) - \psi_{2,w}) dy + A_1 \left(\frac{h_1^2}{2\mu_1} - \frac{h_2^2}{2\mu_2} \right) \right]. \quad (3.13)$$

According to the Nernst–Planck equation, the transport of ions in the channel is described in terms of convection and migration resulting from the pressure difference and electric potential gradient (Wang & Kang 2010), respectively. In addition, the presence of mobile ions along the liquid–liquid interface in such a two-fluid system should be included for the transport of ions. Thus, the current through the channel cross-section is expressed as

$$I = w \int_{-h_2}^{h_1} \rho_e u dy + w \sigma_s u(0) + w \int_{-h_2}^{h_1} \sum_i e z_i n_i v_i E_s dy + G_w (-\Delta\phi). \quad (3.14)$$

Here, the first term is the contribution from convection; the second one characterizes the contribution of mobile ions at the interface; the third is the electro-migration of ions; the last term is added to account for the conductance of the Stern layer near the wall that is denoted by G_w ; the ion mobility $v_i = e z_i D_i / k_B T$ (i.e. the Nernst–Einstein equation); and D_i is the diffusivity of the ion. The diffusivity and mobility of the ion may vary in fluids 1 and 2. Based on the Stokes–Einstein relationship (Masliyah & Bhattacharjee 2006), we propose that the diffusivity of the cations and anions in different fluids is inversely proportional to the viscosity of the

fluid, i.e. $D_{+,1}/D_{+,2} = D_{-,1}/D_{-,2} = \mu_r$. Furthermore, we have considered identical values of the diffusivity ratio ν_r of the cations to the anions in both fluids 1 and 2, i.e. $D_{+,1}/D_{-,1} = D_{+,2}/D_{-,2} = \nu_r$.

Substituting the velocity (3.10) into (3.14) yields the other two phenomenological coefficients L_{21} and L_{22} (see appendix B for the detailed derivation); here L_{21} is found to be the same as L_{12} , which shows the validity of the Onsager reciprocal relation for two-fluid systems; and L_{22} is given by

$$L_{22} = \frac{w\varepsilon_1^2}{lh\mu_2} \left(\frac{k_B T}{ze} \right)^2 \left[\mu_r f_1 + \varepsilon_r f_2 - \bar{A}_1^2 (H_2 + \mu_r H_1) - \frac{ez\mu_2\nu_{-,1}}{2\varepsilon_1 k_B T} K^2 f_3 \right] + G_w, \quad (3.15)$$

with

$$\left. \begin{aligned} f_1 &= H_1 \bar{\sigma}_1^2 + 2K^2 \left[\int_0^{H_1} \cosh(\Psi) dY - H_1 \cosh(\Psi_{1,w}) \right], \\ f_2 &= H_2 \bar{\sigma}_2^2 + 2B^2 \left[\int_{-H_2}^0 \cosh(\Psi) dY - H_2 \cosh(\Psi_{2,w}) \right], \\ f_3 &= \int_0^{H_1} [\nu_r \exp(-\Psi) + \exp \Psi] dY + b\mu_r^{-1} \int_{-H_2}^0 [\nu_r \exp(-\Psi) + \exp \Psi] dY, \\ B &= \sqrt{\frac{b}{\varepsilon_r}} K, \quad \bar{A}_1 = \frac{ezh}{\varepsilon_1 k_B T} A_1. \end{aligned} \right\} \quad (3.16)$$

Here, the non-dimensional height (H_1 , H_2), electric potential (Ψ , $\Psi_{1,w}$, $\Psi_{2,w}$) and surface charge density ($\bar{\sigma}_1$, $\bar{\sigma}_2$) have been used. The expressions for L_{11} and L_{12} are readily rewritten in terms of these non-dimensional variables. It can be observed that the interface charge density σ_s is absent in the expressions for L_{11} , L_{12} and L_{22} , though it appears in expression (3.14) for the current. This indicates that σ_s only has an indirect effect on electrokinetic energy conversion by affecting the distribution of electric potential in the EDLs (see figure 3). This can be explained by the fact that the motion of mobile interfacial charges is compensated by the motion of the counter-ions in the interface Stern layer.

4. Results and discussion

In order to calculate the generation power and energy conversion efficiency of a two-fluid nanofluidic device, the properties of the electrolyte media need to be specified. For illustrative computations, we consider oil–water two-fluid systems, where the liquid in the oil phase is a medium of low dielectric constant compared with the water phase. Concretely, fluid 1 is considered to be water with $\varepsilon_1 = 79 \times (8.854 \times 10^{-12}) \text{ C}^2 \text{ J}^{-1} \text{ m}^{-1}$ and $\mu_1 = 0.93 \times 10^{-3} \text{ kg m}^{-1} \text{ s}^{-1}$ at room temperature $T = 296.15 \text{ K}$. Fluid 2 is the oil phase with large or small viscosity, relative to the water phase. We will discuss two scenarios according to the viscosity of the oil phase. Other physical properties used in the analysis are as follows. The electronic charge $e = 1.602 \times 10^{-19} \text{ C}$ and the Boltzmann constant $k_B = 1.381 \times 10^{-23} \text{ J K}^{-1}$. The length (l) and width (w) of the channel are 4.5 mm and 50 μm , respectively, which are much larger than the height (h). For simplicity, the electrolyte ions are assumed to be monovalent ($z = 1$). As an example, we choose the diffusivity of potassium ions in water at room temperature as the diffusivity of the

electrolyte anions in fluid 1, i.e. $D_{-,1} = 1.96 \times 10^{-9} \text{ m}^2 \text{ s}^{-1}$ (Daiguji *et al.* 2004a,b). The diffusivity ratio ν_r of the cations to the anions varies from 0.2 to 4.759 for typical ions (Barry & Lynch 1991). The charge density σ_1 of a glass/silica surface with water solution is assumed to be -8.2 mC m^{-2} (van der Heyden *et al.* 2007), while $\sigma_2 = 0 \text{ mC m}^{-2}$ is used for the oil–glass/silica surface (Gopmandal & Ohshima 2017).

There is a lot of experimental evidence suggesting that OH^- and other negative ions in water are adsorbed onto oil–water interfaces (e.g. Marinova *et al.* 1996; Gu & Li 1998). The accumulation of negative ions at the liquid–liquid interface is responsible for the arrival of surface charge at the interface, which is balanced by a charge of equal magnitude and opposite sign in the electrolyte solution. Moreover, the redistribution of ions forms an EDL structure, similar to the case of a solid–liquid interface. For a given interface, the interface charge density σ_s depends on the bulk ionic concentration n_∞ and the surface potential ψ_s . Generally, this relationship can be expressed through the Grahame equation (Movahed *et al.* 2012)

$$\sigma_s = \sqrt{8\epsilon k_B T n_\infty} \sinh\left(\frac{ze\psi_s}{2k_B T}\right), \quad (4.1)$$

for symmetric ($z : z$) electrolyte solution. The experimental results from Marinova *et al.* (1996) indicated that the magnitude of the surface charge depends mostly on the composition of the aqueous phase, while the nature of the oil phase is of secondary importance. Therefore, we only focus on the interface charge density on the water side, while ignoring that on the oil side. Again from Marinova *et al.* (1996), the measured surface potential ψ_s is within -50 to -60 mV at the NaCl concentration $n_\infty = 1$ mM (pH = 6), and within -20 to -30 mV at $n_\infty = 10$ mM. The results are not sensitive to the oil type. Using these data and (4.1), one finds that the interface charge density σ_s ranges from -4.2 to -5.3 mC m^{-2} at a concentration $n_\infty = 1$ mM, and from -4.6 to -7.2 mC m^{-2} at $n_\infty = 10$ mM. Furthermore, surfactants can significantly affect the interfacial charge (Marinova *et al.* 1996; Gu & Li 1998). To extend our analysis, the range of σ_s is assumed to be from 0 to -10 mC m^{-2} at $n_\infty = 1$ mM, while it is from 0 to -15 mC m^{-2} at $n_\infty = 10$ mM in this paper. Thus, the ranges of the interface charge density are different for different salt concentrations.

The potential drop across the water–organic solution interface was measured by Conboy & Richmond (1997), and ranges from -0.48 V to 0.45 V. This value may be affected by the interface location and the surface charge on the walls. However, these influences are not available in the literature, and lack in-depth research, especially in nanoscale channels. In this paper, we consider that the interface potential difference is between -0.104 and 0.104 V. Since the oil and water are in different phases, the penetration of electrolyte ions through the oil phase will occur through a discontinuous manner with non-unit partition coefficient of electrolyte ions. The effect of ion partition coefficient on electrokinetic energy conversion will also be investigated.

In this study, we first numerically solved the EDL electric potential distribution within fluids 1 and 2. Then, a direct numerical integration approach was applied to compute the phenomenological coefficients L_{11} , L_{12} and L_{22} . Thus the figure of merit α , thereby the generation power and efficiency, can be determined. Here we use the expressions in (2.4) to calculate the generation power and energy conversion efficiency. Note that the expressions in (2.5) will give almost the same results due to small α for practical electrokinetic energy converters. In order to verify the present numerical framework, we have made a comparison with the experimental data. The

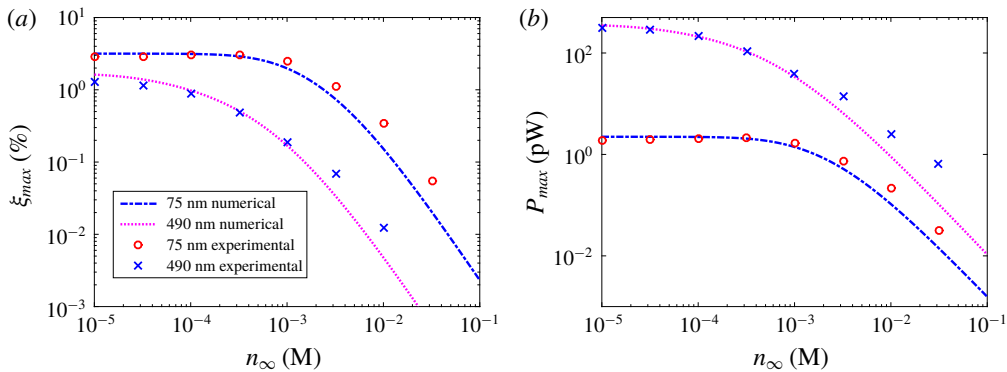


FIGURE 2. (Colour online) Dependence of (a) maximum energy conversion efficiency and (b) maximum electrokinetic power output in a silica nanochannel on the salt concentration n_{∞} , under $\Delta p = -4$ bar. Symbols: experimental data of KCl solution from van der Heyden *et al.* (2007) at $h = 75$ and 490 nm. Curves: calculated results of our model without the interface potential difference and the interface charge density jump, where the surface charge densities $\sigma_1 = \sigma_2 = -8.2$ mC m $^{-2}$; G_w was 16 and 22 pS for $h = 75$ and 490 nm, respectively.

generation power and energy conversion efficiency of two-layer fluids with the same viscosities and permittivities can be compared with the case of a single-layer fluid, when the interface potential difference and the interface charge density jump vanish. Figure 2 shows the consistency between the numerical results and the experimental data. Furthermore, it is observed that the power and efficiency are the highest in the low-salt regime.

4.1. Oil phase with large viscosity

In the first scenario, fluid 2 is considered to be an oil phase with large viscosity and low permittivity, such as cyclohexyl bromide (CHB) with $\varepsilon_2 = 7.9 \times (8.854 \times 10^{-12})$ C 2 J $^{-1}$ m $^{-1}$ and $\mu_2 = 2.269 \times 10^{-3}$ kg m $^{-1}$ s $^{-1}$ (Gopmandal & Ohshima 2017), compared with the aqueous phase in fluid 1. That implies $\varepsilon_r < 1$ and $\mu_r > 1$. Furthermore, the value of the ion partition coefficient b is considered to be less than unity, as the electrolyte ions always tend to remain in the medium with high dielectric constant (Ohshima *et al.* 1985).

In figure 3, we display the dimensionless net charge density and electrostatic potential profiles in the two-fluid system. It can be found that the net charge density in the oil phase is much less than that in the aqueous phase due to the ion partitioning effect that reduces the salt concentration in the oil layer. Thus, the EDL effect in the oil layer is not remarkable relative to the aqueous solution. In addition, there is a peak near the liquid–liquid interface, which depends on the interface charge density σ_s . The magnitudes of net charge density and potential in the two-fluid system increase significantly with the increase of $|\sigma_s|$.

Figure 4 displays the variations of the dimensionless velocity $U = 2\mu_1 l u / (-\Delta p)$ with the interface charge density for different interface locations, where $H_1 = 1 - H_2$ represents the dimensionless thickness of the aqueous layer. Note that $\sigma_2 = 0$ mC m $^{-2}$, and thus the Stern conductance near the oil–glass/silica surface can be disregarded; thereby the wall Stern conductance G_w of the whole two-layer fluid system is reduced.

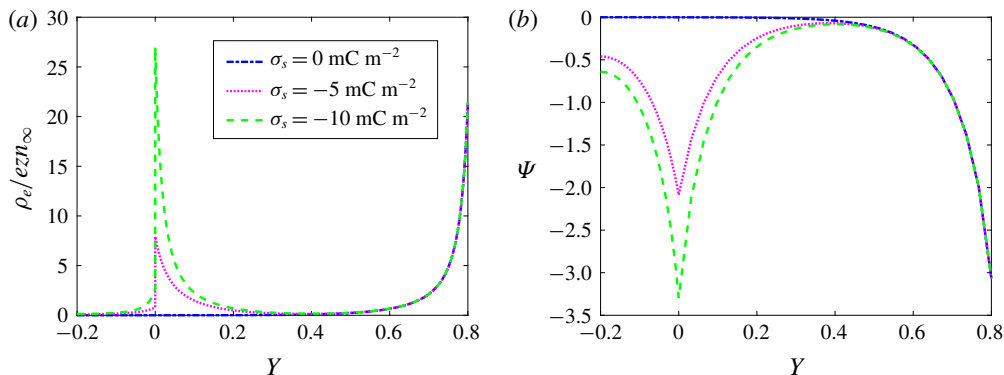


FIGURE 3. (Colour online) Profiles of the dimensionless (a) net charge density and (b) electrostatic potential in a two-fluid system for different interface charge density, where $h = 100 \text{ nm}$, $n_\infty = 1 \text{ mM}$, $\Delta\psi = 0 \text{ V}$, the partition coefficient $b = 0.1$, and the dimensionless thicknesses of the aqueous phase and oil phase are 0.8 and 0.2 respectively.

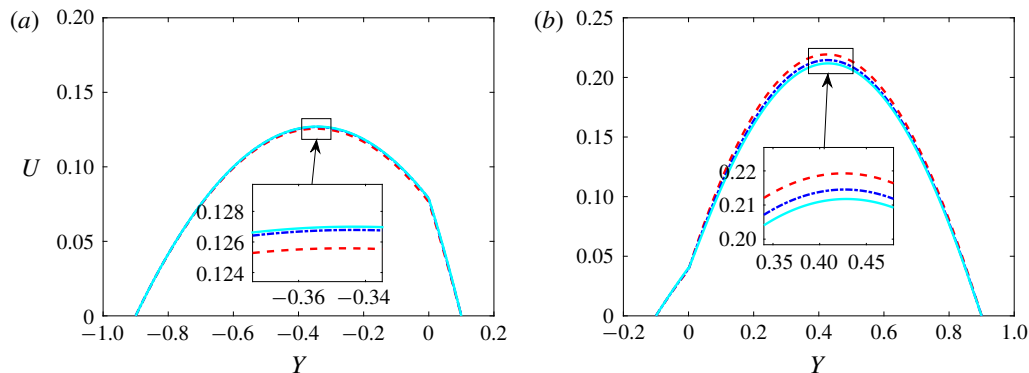


FIGURE 4. (Colour online) Profiles of the dimensionless velocity U across the channel for interface charge density $\sigma_s = 0$ (dashed line), -5 (dash-dotted line) and -10 (solid line) with (a) relatively thick oil layer ($H_1 = 0.1$) and (b) relatively thin oil layer ($H_1 = 0.9$). The other parameters are $h = 100 \text{ nm}$, $\Delta\psi = 40 \text{ mV}$, $n_\infty = 1 \text{ mM}$, $G_w = 11 \text{ pS}$, the ratio $\nu_r = 0.25$ and the ion partition coefficient $b = 0.1$. Insets show local enlarged drawings.

In this paper, G_w is assumed to be 11 pS. Comparing figure 4(a) with figure 4(b), it can be seen that an increase in the relative thickness of the oil layer leads to a decrease in the velocity across the channel because of the large viscosity of the oil (CHB). The role of interfacial charges is also investigated. In the case of a thin oil layer (i.e. large H_1), the interfacial charge has a retardation effect on the fluid velocity; while for a thick oil layer (i.e. small H_1), the opposite effect (i.e. enhanced effect) is observed.

As stated in § 2, the figure of merit α gauges the performance of electrokinetic energy converters, and the maximum generation efficiency is a monotonically increasing function of α . The variations of α against σ_s are demonstrated in figure 5(a) for different values of dimensionless thickness H_1 . It can be seen that the presence of a relatively thin oil layer (large H_1) tends to increase the value of α with the interfacial charge, thereby improving the energy conversion efficiency. While, for a

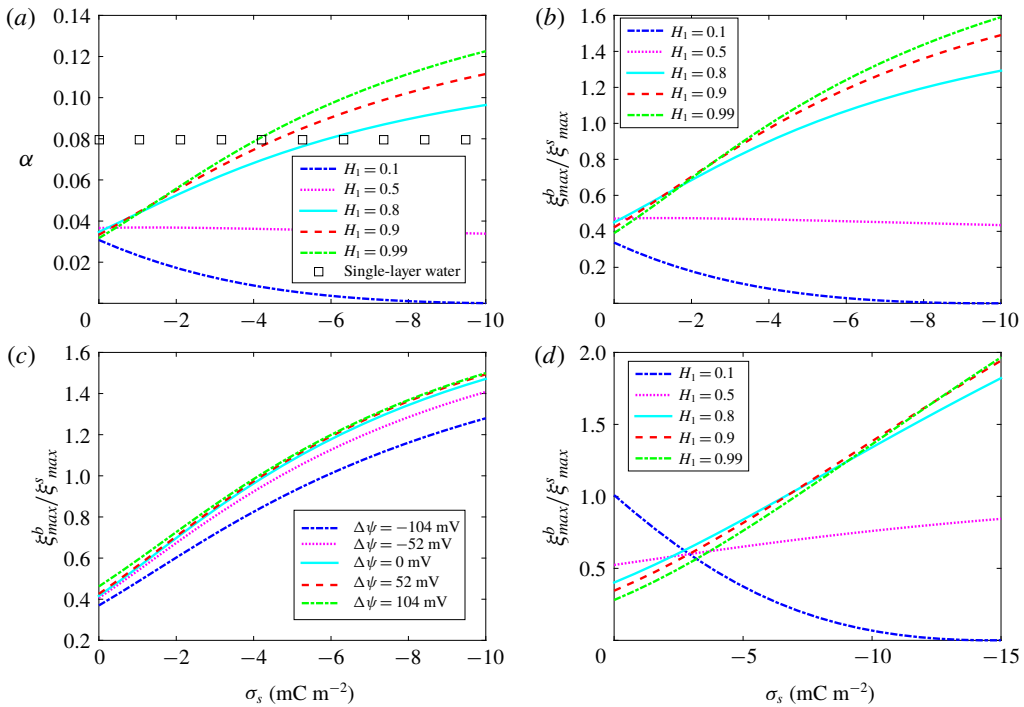


FIGURE 5. (Colour online) (a) Variations of α against the interface charge density for different values of dimensionless thickness H_1 . Here $h = 100$ nm, $\Delta\psi = -40$ mV, $n_\infty = 1$ mM, $G_w = 11$ pS, the ratio $\nu_r = 0.25$ and the partition coefficient $b = 0.01$. Note that the value of α in single-phase flow is also plotted for comparison. (b) Same as (a) but for the variations of the efficiency ratio. (c) Variations of the efficiency ratio with σ_s for different values of $\Delta\psi$. Here $h = 100$ nm, $n_\infty = 1$ mM, $G_w = 11$ pS, $\nu_r = 0.25$, $b = 0.01$ and $H_1 = 0.9$. (d) Same as (b) but the bulk ionic concentration $n_\infty = 10$ mM instead of 1 mM, and the range of σ_s is also different due to different ionic concentration.

relatively thick oil layer (small H_1), the opposite trend can be observed with the interfacial charge. This is essentially related to the effect of interfacial charge on the velocity profile, and will be explained from the perspective of energy transfer and dissipation later. Furthermore, for the case of a thin oil layer (e.g. $H_2 = 1 - H_1 < 0.2$), the value of α is more than that in single-phase flow for moderate and large interface charge densities (e.g. $|\sigma_s| > 4$ mC m^{-2}). This implies that the efficiency of such a two-fluid energy converter may exceed that of a single-phase flow system. The efficiency ratio can be defined by the ratio of maximum efficiency in binary flow to that in single-phase flow (i.e. $\xi_{max}^b / \xi_{max}^s$), and the results obtained in our scenario are demonstrated in figure 5(b). From these figures, we can see that the maximum efficiency in the two-fluid flow will increase with the increase of $|\sigma_s|$ for a thin oil layer. The maximum efficiency can be up to 1.5 times that of the single-phase flow system in the range of σ_s .

Figure 5(c) illustrates how the energy conversion efficiency ratio varies with the interface charge density σ_s for different interface potential difference $\Delta\psi$ at fixed $H_1 = 0.9$. We find that a positive $\Delta\psi$ tends to increase the conversion efficiency and a negative one reduces the efficiency. This can be explained by associating the interface

potential difference $\Delta\psi$ with the distribution of the charges. To be specific, a positive $\Delta\psi$ will increase the net charge density in the EDL formed at the liquid–liquid interface, thereby increasing the streaming current and the conversion efficiency; while a negative $\Delta\psi$ has the opposite effect (data not shown). In the high-salt regime, the efficiency of a single-fluid system decreases significantly because of the power dissipation caused by ionic conductance (van der Heyden *et al.* 2007). In contrast, the ion partitioning effect in a two-fluid system reduces the salt concentration within the oil layer, thereby reducing the electrical conductivity. Therefore, the combined effects of interfacial charge and ion partitioning may be used to improve the performance of electrokinetic energy converters at high salt. Figure 5(d) displays the variations of the efficiency ratio at the bulk ionic concentration $n_\infty = 10$ mM. In our calculations, the efficiency of the two-fluid energy converter can be up to twice that of the single-phase flow system when a thin oil layer is added. Similarly, the presence of interfacial charge in the two-fluid flow also augments the maximum generation power. The maximum powers can be up to 1.5 and 2 times that of the single-phase flow system at $n_\infty = 1$ mM and 10 mM, respectively. The corresponding figures are not shown here.

From the viewpoint of energy transfer, the input power, produced by the pressure work, is converted into three parts: output power, viscous dissipation and electrical Joule heating dissipation. In order to further investigate the performance of the two-fluid energy converter, we show the variations of the viscous dissipation (denoted by P_V) and electrical Joule heating dissipation (denoted by P_E) with σ_s for different values of dimensionless thickness H_1 in figure 6. The power consumed by viscous and electrical Joule heating can be derived by a combined thermodynamic and fluid mechanics analysis on the system, which is given in appendix C. From figure 6, it can be seen that viscous dissipation consumes most of the power (more than 90% of the total power input), whether it is in binary or single flows (figure 6d). This is a major factor limiting the efficiency of electrokinetic energy converters. In contrast to the single-phase flows of water solution, the addition of a thin oil layer reduces viscous dissipation for moderate or high interfacial charge density (figure 6b,d), due to the retardation effect of the interfacial charge on the fluid velocity (see figure 4b). While in the case of a relatively thick oil layer, the ratio of the viscous dissipation to the input power increases with the interfacial charge, because of the enhanced effect of the interfacial charge on the fluid velocity (see figure 4a). Thus, a thin oil layer tends to increase the energy conversion efficiency with the interfacial charge, and a thick oil layer has the opposite trend, which explains the effect of interface location on the energy conversion efficiency in figure 5. It is noteworthy that, although the presence of interfacial charges leads to an increase in electrical Joule heating dissipation, the amount of the increased power consumption is less than that of the reduced viscous dissipation in the case of thin oil layers (e.g. $H_1 = 0.9$ in figure 6c,d). Therefore, the total consumption of power is reduced and the efficiency is improved.

4.2. Oil phase with small viscosity

In the second scenario, we consider fluid 2 to be an oil phase with low viscosity and permittivity, such as octane with $\varepsilon_2 = 2.0 \times (8.854 \times 10^{-12}) \text{ C}^2 \text{ J}^{-1} \text{ m}^{-1}$ and $\mu_2 = 0.566 \times 10^{-3} \text{ kg m}^{-1} \text{ s}^{-1}$ (Lee *et al.* 2006), relative to the aqueous phase in fluid 1. That implies $\mu_r < 1$. Figure 7(a) displays the profiles of the dimensionless velocity U for different interface charge densities and interface locations (characterized by H_1). Because of the relatively small viscosity of the oil (octane), the increase in

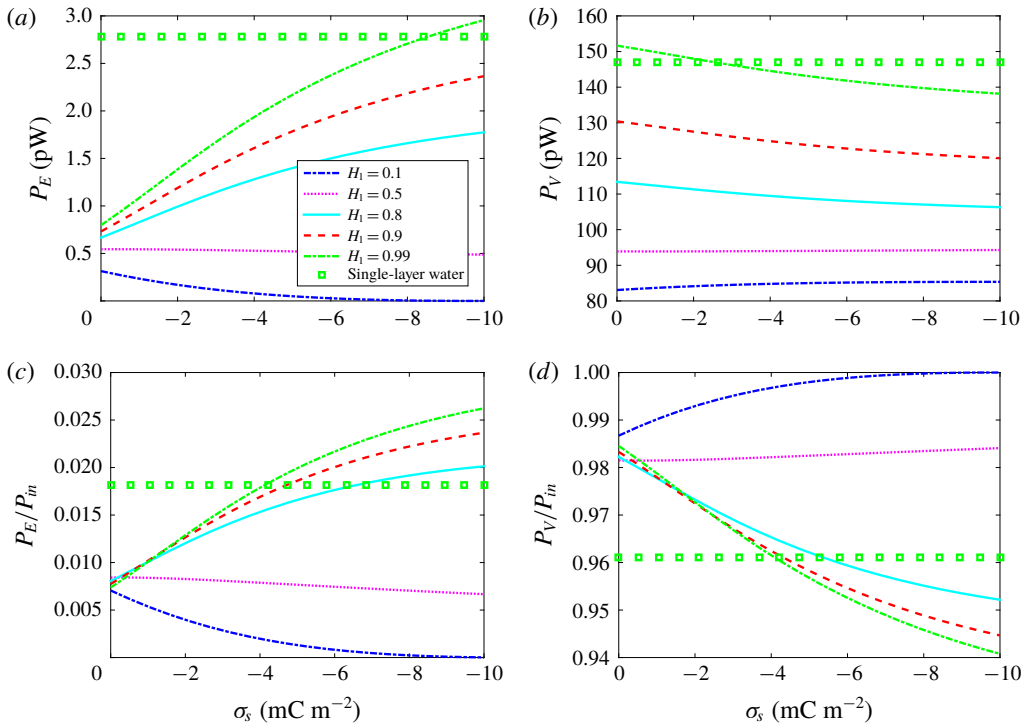


FIGURE 6. (Colour online) Variations of (a) the electrical Joule heating dissipation (denoted by P_E) and (b) viscous dissipation (denoted by P_V) with the interface charge density σ_s for different values of dimensionless thickness H_1 in two-fluid flows. (c,d) Variations of the ratio of (c) the electrical Joule heating dissipation to the power input (P_E/P_{in}) and (d) viscous dissipation to the power input (P_V/P_{in}) with σ_s . Here $h = 100$ nm, $\Delta\psi = 40$ mV, $n_\infty = 1$ mM, $G_w = 11$ pS, $\Delta p = -4$ bar, the ratio $\nu_r = 0.25$ and the partition coefficient $b = 0.01$. The symbol represents the corresponding value in single-phase flow of water solution, which is a constant independent of the interfacial charges.

the thickness of the oil layer (i.e. small H_1) leads to an increase of the velocity across the channel. That is different from the case of $\mu_r > 1$ (see figure 4). On the other hand, the interfacial charge has different effects (enhanced or weakened) on the fluid velocity for different interface locations, which is similar to the case of $\mu_r > 1$. The variations of the figure of merit α with σ_s are demonstrated in figure 7(b) against different values of H_1 . Compared with the single-phase flow, the presence of a relatively thin oil layer (e.g. $H_2 = 1 - H_1 < 0.1$) can increase the value of α for large interfacial charges, thus improving the energy conversion efficiency.

Variations of the ratio of maximum efficiency in binary flow to that in single-phase flow are demonstrated in figure 8 at different salt concentrations in the case of $\mu_r < 1$. One finds that the maximum efficiency can be up to 1.5 times that of the single-phase flow system for a relatively thin oil layer at the salt concentration $n_\infty = 1$ mM. While, in the high-salt regime (e.g. $n_\infty = 10$ mM), the efficiency of the two-fluid energy converter can be up to 2 times that of the single-phase flow system due to the combined effects of interfacial charge and ion partitioning. Meanwhile, the maximum generation power in the two-fluid flow is also augmented due to the presence of

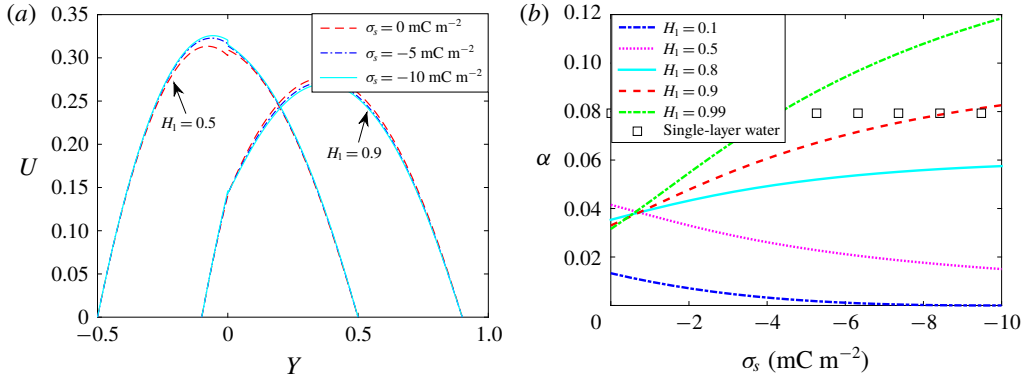


FIGURE 7. (Colour online) (a) Profiles of the dimensionless velocity U across the channel for different values of interface charge density σ_s and the dimensionless thicknesses H_1 . (b) Variations of the figure of merit α with the interface charge density σ_s against different values of dimensionless thickness H_1 . Here $h = 100 \text{ nm}$, $\Delta\psi = 40 \text{ mV}$, $n_\infty = 1 \text{ mM}$, $G_w = 11 \text{ pS}$, the ratio $\nu_r = 0.25$ and the partition coefficient $b = 0.01$. Note that the value of α in single-phase flow is also plotted in this panel for comparison.

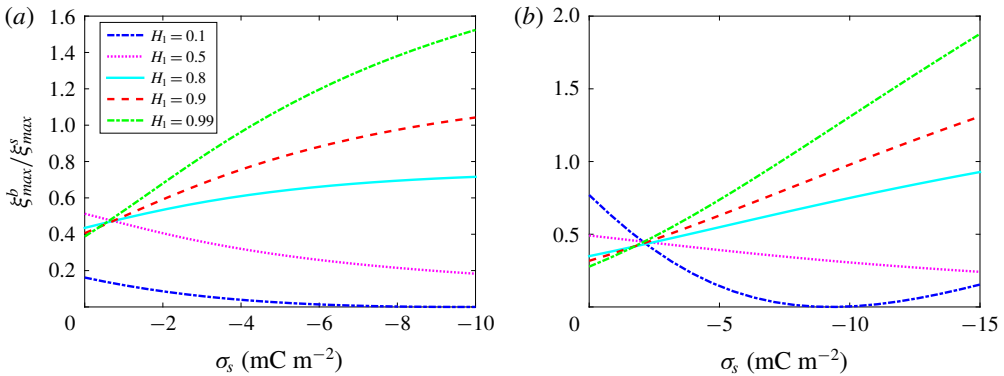


FIGURE 8. (Colour online) Variations of the efficiency ratio in two-fluid flow to that in single-phase flow in the case of $\mu_r < 1$. The values of the parameters are the same as in figure 5 except for (a) $n_\infty = 1 \text{ mM}$ and (b) $n_\infty = 10 \text{ mM}$.

interfacial charges. The maximum power will increase 1.5 and 2 times compared with the single-phase flow system at $n_\infty = 1 \text{ mM}$ and 10 mM , respectively, when a relatively thin oil layer is added (the corresponding figures are not shown here). These results indicate that whether $\mu_r > 1$ or $\mu_r < 1$, the influence of interfacial charges on electrokinetic energy conversion are similar in the limit of a relatively thin oil layer.

Furthermore, we investigate the performance of a two-fluid energy converter from the viewpoint of energy transfer for the case of $\mu_r < 1$. In figure 9, we show the variations of the viscous dissipation P_V and electrical Joule heating dissipation P_E with the interface charge density for different interface locations. In contrast to the case of $\mu_r > 1$, the addition of an oil layer results in an increase of viscous dissipation (figure 9b) because of the increased velocity. But the ratio of viscous dissipation to total power input is reduced for thin oil layers and large interface charge density (see

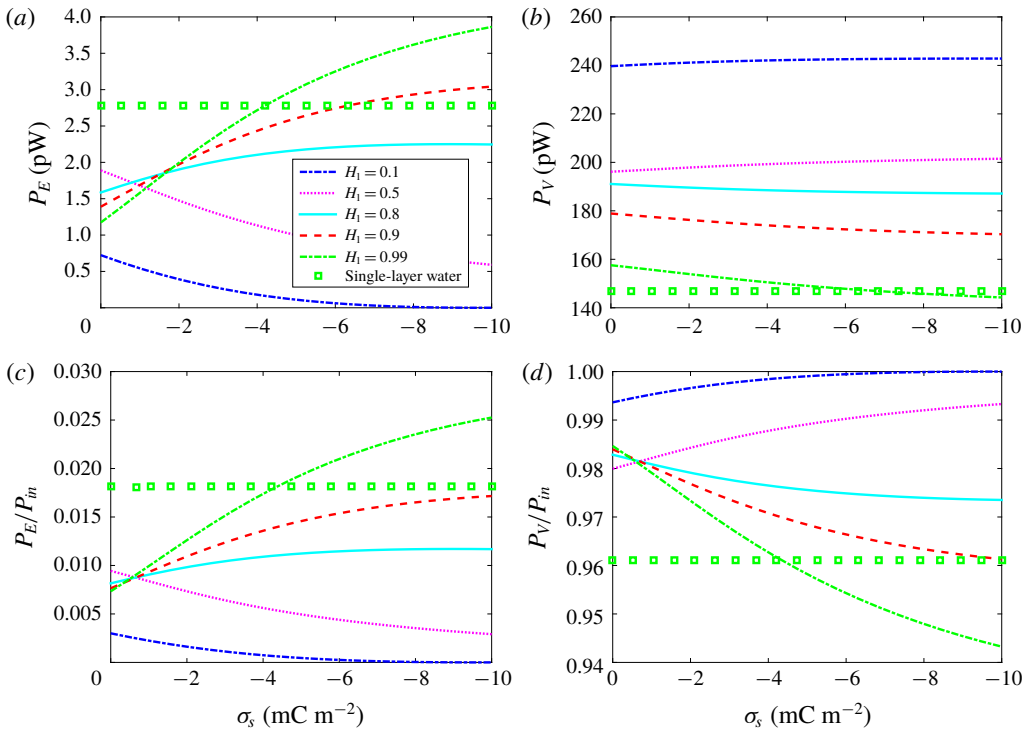


FIGURE 9. (Colour online) Variations of (a) the electrical Joule heating dissipation P_E and (b) viscous dissipation P_V with the interface charge density σ_s for different values of dimensionless thickness H_1 in the case of $\mu_r < 1$. (c,d) Variations of the ratio of (c) the electrical Joule heating dissipation to the power input (P_E/P_{in}) and (d) viscous dissipation to the power input (P_V/P_{in}). Here the values of other parameters are the same as in figure 6. The symbol represents the corresponding value in single-phase flow of water solution, which is a constant independent of the interfacial charges.

figures 9d and 11b). This is essentially due to the retardation effect of interfacial charges on the fluid velocity in the case of a thin oil layer (see figure 7a). Note that at the same time the presence of interfacial charges leads to an increase in electrical Joule heating dissipation for thin oil layers and large interface charge density (see figure 9a,c). However, the increased ratio of the Joule heating dissipation to the power input is less than the reduced one of the viscous dissipation to the power input. Therefore, a conclusion similar to the case of $\mu_r > 1$ can be obtained, i.e. the addition of a thin oil layer reduces the total consumption of power and improves the efficiency.

5. Conclusion

In this study, we first show the equivalence between thermodynamic analysis and circuit analysis for the calculations of output powers and conversion efficiencies under the maximum power generation and/or maximum conversion efficiency conditions in the linear response regime. Then, we present a nanofluidic energy conversion system consisting of two-layer fluids. Semi-analytical expressions of the velocity, induced current and energy transfer efficiency are obtained where the roles of the interfacial

charge, zeta potential jump, finite conductance of the Stern layer, and ion partitioning have been included. Meanwhile, the validity of the Onsager reciprocal relation to such a two-fluid flow has been verified.

As illustrative calculations, we consider two concrete oil–water two-fluid systems with different properties, and find that the magnitude of the interfacial charges and the location of the interface have significant effects on electrokinetic energy conversion. Qualitatively, for negatively charged interfaces, the addition of a relatively thin oil layer can increase the value of the figure of merit α for moderate and large interfacial charge densities, thus improving the energy conversion efficiency. Furthermore, the thinner the oil layer and the larger the interfacial charge densities, the greater the energy conversion efficiency. While for a relatively thick oil layer, the presence of a negative interface charge has the opposite effect (i.e. reduction effect) on the energy conversion efficiency in the ranges of the parameters. Additionally, in the high-salt regime, the ion partitioning effect in two-fluid systems reduces the salt concentration within the oil layer, thereby reducing the electrical dissipation and further improving the efficiency. Quantitatively, in our calculations, the maximum efficiency increases 1.5 and 2 times relative to the single-phase flow system at $n_\infty = 1$ and 10 mM, respectively, when restricted to thin oil layers. This enhancement depends strongly on the magnitude of mobile charges present at the oil–water interface and the interface location, not on the viscosity ratio of oil to water (i.e. $\mu_r > 1$ or $\mu_r < 1$). The same results can also be obtained for the maximum generation power. These phenomena have been analysed and explained from the perspective of energy transfer.

The input power produced by the pressure work is converted into three parts: output power, viscous dissipation and electrical Joule heating dissipation. The viscous dissipation consumes most of the power (more than 90%), in both single-phase and two-fluid flows. However, the ratio of the viscous dissipation to the power input decreases with increase of the interfacial charge density for the case of a relatively thin oil layer in two-fluid flows, which is essentially due to the retardation effect of interfacial charges on the fluid velocity. The efficiency of such a two-fluid energy converter increases with the interfacial charge density, and is higher than that of the single-phase flow system for moderate and high interfacial charge densities. On the other hand, for the case of a relatively thick oil layer, the ratio of the viscous dissipation to the power input increases with the interfacial charge density due to the enhanced effect of interfacial charges on the fluid velocity, and the efficiency decreases.

Acknowledgements

We acknowledge financial support from the National Natural Science Foundation of China (grant nos. 11772162, 11472140), the Natural Science Foundation of Inner Mongolia Autonomous Region of China (grant no. 2016MS0106) and the Inner Mongolia Grassland Talent (grant no. 12000-12102013). We are also grateful to the anonymous referees for their comments and suggestions that greatly improved the paper.

Appendix A. Numerical algorithm for electrical double-layer potential

The nonlinear differential equation (3.6) with the boundary conditions (3.7) is solved using a finite difference scheme. The domain of $\Psi(Y)$ is the interval $[-H_2, H_1]$; $Y_j = -H_2 + j\Delta Y_2$ ($j = 0, 1, \dots, N_2$) and $Y_{N_2+j} = j\Delta Y_1$ ($j = 0, 1, \dots, N_1$) are regarded as discrete grid points in the intervals $[-H_2, 0]$ and $[0, H_1]$, respectively, where the step

sizes are $\Delta Y_2 = H_2/N_2$ and $\Delta Y_1 = H_1/N_1$; and $N_1 + N_2 + 2$ is the total number of grid points. We let $\Psi_{2,j} = \Psi(Y_j)$ ($j = 0, 1, \dots, N_2$) and $\Psi_{1,j} = \Psi(Y_{N_2+j})$ ($j = 0, 1, \dots, N_1$) approximate the distribution of EDL potential in fluids 2 and 1, respectively; then $\Psi_{2,0}$ and Ψ_{1,N_1} represent the wall zeta potentials of the lower and upper plate, respectively. Applying the second-order central difference scheme to the left-hand side of the equations and the linearization approximation to the right-hand side of the equations yields

$$\Psi_{2,j+1}^{k+1} + P_2(\Psi_{2,j}^k)\Psi_{2,j}^{k+1} + \Psi_{2,j-1}^{k+1} = Q_2(\Psi_{2,j}^k), \quad j = 0, 1, \dots, N_2, \tag{A 1}$$

$$\Psi_{1,j+1}^{k+1} + P_1(\Psi_{1,j}^k)\Psi_{1,j}^{k+1} + \Psi_{1,j-1}^{k+1} = Q_1(\Psi_{1,j}^k), \quad j = 0, 1, \dots, N_1, \tag{A 2}$$

where k is the iteration index, the functions

$$P_1(\Psi) = -(2 + K^2 \Delta Y_1^2 \cosh \Psi), \quad Q_1(\Psi) = K^2 \Delta Y_1^2 (\sinh \Psi - \Psi \cosh \Psi), \tag{A 3a,b}$$

$$P_2(\Psi) = -(2 + B^2 \Delta Y_2^2 \cosh \Psi), \quad Q_2(\Psi) = B^2 \Delta Y_2^2 (\sinh \Psi - \Psi \cosh \Psi), \tag{A 4a,b}$$

with $B = \sqrt{b/\varepsilon_r}K$ and the partition coefficients $b = b_+ = b_-$.

The corresponding boundary conditions (3.7) are discretized as

$$\Psi_{1,N_1+1}^{k+1} = \Psi_{1,N_1-1}^{k+1} + 2\varepsilon_r \Delta Y_1 \bar{\sigma}_1, \tag{A 5}$$

$$\Psi_{2,-1}^{k+1} = \Psi_{2,1}^{k+1} + 2\Delta Y_2 \bar{\sigma}_2, \tag{A 6}$$

$$\Psi_{2,N_2}^{k+1} - \Psi_{1,0}^{k+1} = \Delta \Psi, \tag{A 7}$$

$$\varepsilon_r \Delta Y_1 (\Psi_{2,N_2}^{k+1} - \Psi_{2,N_2-1}^{k+1}) - \Delta Y_2 (\Psi_{1,1}^{k+1} - \Psi_{1,0}^{k+1}) = \varepsilon_r \Delta Y_1 \Delta Y_2 \bar{\sigma}_s. \tag{A 8}$$

In order to improve the accuracy of the first-order derivative boundary conditions, imaginary electric potentials Ψ_{1,N_1+1}^{k+1} and $\Psi_{2,-1}^{k+1}$ are introduced in (A 5) and (A 6), which can be expressed by using the values of internal points near the walls. Equations (A 7) and (A 8) represent the relationship of the potential at the interface of the two-layer fluids.

Combining (A 1)–(A 8), we derive a series of algebraic equations which can be expressed in matrix form as

$$\begin{pmatrix} P_2(\Psi_{2,0}^k) & 2 & 0 & 0 & \cdot & \cdot & \cdot & 0 \\ 1 & P_2(\Psi_{2,1}^k) & 1 & & & & & \\ 0 & \ddots & \ddots & \ddots & & & & \cdot \\ & & 1 & P_2(\Psi_{2,N_2-1}^k) & 1 & & & \cdot \\ \cdot & & & -\varepsilon_r \Delta Y_1 & \Theta & -\Delta Y_2 & & \cdot \\ \cdot & & & & 1 & P_1(\Psi_{1,1}^k) & 1 & \\ \cdot & & & & & \ddots & \ddots & \ddots \\ & & & & & & 1 & P_1(\Psi_{1,N_1-1}^k) & 1 \\ 0 & & & & & & & 2 & P_1(\Psi_{1,N_1}^k) \end{pmatrix}$$

$$\times \begin{pmatrix} \Psi_{2,0}^{k+1} \\ \Psi_{2,1}^{k+1} \\ \vdots \\ \Psi_{2,N_2-1}^{k+1} \\ \Psi_{2,N_2}^{k+1} \\ \Psi_{1,1}^{k+1} \\ \Psi_{1,2}^{k+1} \\ \vdots \\ \Psi_{1,N_1-1}^{k+1} \\ \Psi_{1,N_1}^{k+1} \end{pmatrix} = \begin{pmatrix} Q_2(\Psi_{2,0}^k) - 2\Delta Y_2 \bar{\sigma}_2 \\ Q_2(\Psi_{2,1}^k) \\ \vdots \\ Q_2(\Psi_{2,N_2-1}^k) \\ \Delta Y_1 \Delta Y_2 \bar{\sigma}_2 + \Delta Y_2 \Delta \Psi \\ Q_1(\Psi_{1,1}^k) + \Delta \Psi \\ Q_1(\Psi_{1,2}^k) \\ \vdots \\ Q_1(\Psi_{1,N_1-1}^k) \\ Q_1(\Psi_{1,N_1}^k) - 2\Delta Y_1 \bar{\sigma}_1 \end{pmatrix}, \tag{A 9}$$

with $\Theta = \varepsilon_r \Delta Y_1 + \Delta Y_2$. This system was solved using a line-by-line iteration scheme combined with a tridiagonal matrix algorithm (TDMA) solver. A constant potential (e.g. $\Psi_{i,j}^0 = -1$) can be used as an initial guess, and the iterations are continued until the relative difference between two successive iterations becomes smaller than the tolerance limit 10^{-5} . The convergence of the algorithm and the sensitivity of results to the number of grid points are shown in table 2. We see that when the number of grid points $N_g (= N_1 + N_2) = 2000$ and the number of iteration steps $N_s = 10$, the relative error of the potential is less than 0.01.

For the single-phase flow of electrolyte solution in a parallel nanofluidic channel, the EDL potential distribution for a symmetric electrolyte solution is represented by (Behrens & Grier 2001)

$$\Psi = \Psi_0 + 2 \ln \operatorname{cd}(u|m), \tag{A 10}$$

$$\bar{\sigma} = K(m^{3/4} - m^{-1/4}) \frac{\operatorname{sn}(u|m)}{\operatorname{cn}(u|m) \operatorname{dn}(u|m)} \Big|_{\text{wall}}. \tag{A 11}$$

Here $u = KY/2 \exp(-\Psi_0/2)$ and $m = \exp(2\Psi_0)$; Ψ_0 is the double-layer potential at the channel centre; $\bar{\sigma}$ is the dimensionless charge density at the walls scaled by $zeh/\varepsilon k_B T$; and $\operatorname{cd}(u|m)$, $\operatorname{sn}(u|m)$, $\operatorname{cn}(u|m)$ and $\operatorname{dn}(u|m) = \operatorname{cn}(u|m)/\operatorname{cd}(u|m)$ are Jacobian elliptic functions of argument u and parameter m . Efficient numeric implementations of these functions are readily available from MATLAB software. Furthermore, if the EDLs are not overlapped, the wall charge density and zeta potential can also be related by the Grahame equation (Wang & Kang 2010)

$$\bar{\sigma} = 2K \sinh(\Psi_w/2), \tag{A 12}$$

with Ψ_w the wall zeta potential.

In order to verify the above numerical solution, we have made a comparison with the analytical solution (A 10)–(A 12). Here fluids 1 and 2 are assumed to be the same fluid; the interface potential difference and the interface charge density jump vanish. A good consistency of the EDL potential distribution under different salt concentrations can be observed in figure 10.

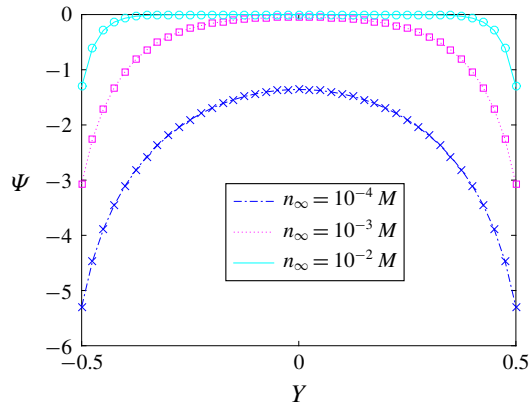


FIGURE 10. (Colour online) Profiles of the normalized EDL potential under different salt concentrations n_∞ , where fluids 1 and 2 are the same. Symbols: analytical solution from (A 10)–(A 12). Curves: numerical solution without the interface potential difference and the interface charge density jump. The surface charge densities $\sigma_1 = \sigma_2 = -8.2 \text{ mC m}^{-2}$, and $h = 90 \text{ nm}$.

N_g	N_s				
	1	5	10	15	20
100	1.4699	0.6347	0.2420	0.2420	0.2420
500	1.2937	0.4551	0.0385	0.0385	0.0385
1000	1.2725	0.4338	0.0166	0.0166	0.0166
2000	1.2620	0.4232	0.0062	0.0062	0.0062
3000	1.2585	0.4197	0.0027	0.0027	0.0027

TABLE 2. Relative error of the potential profile for different numbers of iteration steps N_s and grid points N_g ($= N_1 + N_2$) for the typical parameters: $\sigma_1 = -8.2 \text{ mC m}^{-2}$, $\sigma_2 = 0 \text{ mC m}^{-2}$, $\sigma_s = -15 \text{ mC m}^{-2}$, $n_\infty = 10^{-3} \text{ M}$, $\Delta\psi = 0 \text{ V}$, $b = 0.01$, $\nu_r = 0.25$, $\varepsilon_r = 0.1$ and $H_1 = 0.9$.

Appendix B. Analytical derivations of phenomenological coefficients L_{21} and L_{22}

Under the assumption $b_+ = b_- = b$, equation (3.6) can be rewritten as

$$\frac{d^2\Psi}{dY^2} = \begin{cases} K^2 \sinh \Psi, & 0 < Y < H_1, \\ B^2 \sinh \Psi, & -H_2 < Y < 0, \end{cases} \quad (\text{B } 1)$$

with $B = \sqrt{b/\varepsilon_r}K$. Multiplying by $d\Psi/dY$ and integrating (B 1), we get

$$\left(\frac{d\Psi}{dY}\right)^2 \Big|_{Y=H_1} - \left(\frac{d\Psi}{dY}\right)^2 = 2K^2[\cosh(\Psi_{1,w}) - \cosh \Psi], \quad 0 < Y < H_1, \quad (\text{B } 2)$$

$$\left(\frac{d\Psi}{dY}\right)^2 - \left(\frac{d\Psi}{dY}\right)^2 \Big|_{Y=-H_2} = 2B^2[\cosh \Psi - \cosh(\Psi_{2,w})], \quad -H_2 < Y < 0. \quad (\text{B } 3)$$

Using the boundary conditions (3.7), we derive

$$\left(\frac{d\psi}{dY}\right)^2 = \begin{cases} \bar{\sigma}_1^2 + 2K^2[\cosh(\Psi_{1,w}) - \cosh \Psi], & 0 < Y < H_1, \\ \bar{\sigma}_2^2 + 2B^2[\cosh \Psi - \cosh(\Psi_{2,w})], & -H_2 < Y < 0, \end{cases} \tag{B 4}$$

where $\Psi_{1,w}$ and $\Psi_{2,w}$ are the normalized double-layer potentials of the upper wall and lower wall, respectively.

The total electric current in (3.14) along the slit nanochannel of height h and width w can be rewritten as

$$I = -w\epsilon_1 I_1 - w\epsilon_2 I_2 + w\sigma_s u(0) - ezw \frac{\Delta\phi}{l} I_3 + G_w(-\Delta\phi), \tag{B 5}$$

where

$$I_1 = \int_0^{h_1} \frac{d^2\Psi}{dy^2} dy, \tag{B 6}$$

$$I_2 = \int_{-h_2}^0 \frac{d^2\Psi}{dy^2} dy, \tag{B 7}$$

$$I_3 = \int_{-h_2}^{h_1} (n_+ v_+ - n_- v_-) dy. \tag{B 8}$$

Substituting the velocity (3.10) into (B 6) and integrating by parts gives

$$\begin{aligned} I_1 = & \frac{\Delta\phi}{l\mu_1} \left[(h_1 A_1 - \epsilon_1 \psi_{1,w} + \epsilon_1 \psi(0^+)) \frac{d\psi}{dy} \Big|_{y=0^+} - A_1(\psi_{1,w} - \psi(0^+)) \right. \\ & + \epsilon_1 \int_0^{h_1} \left(\frac{d\psi}{dy}\right)^2 dy \Big] + \frac{\Delta p}{2l\mu_1} \left[h_1(h_1 + A_2) \frac{d\psi}{dy} \Big|_{y=0^+} - \psi_{1,w}(2h_1 + A_2) \right. \\ & \left. + \psi(0^+)A_2 + 2 \int_0^{h_1} \psi(y) dy \right]. \end{aligned} \tag{B 9}$$

Using these dimensionless variables in (3.5) and equation (B 4), I_1 reduces to

$$\begin{aligned} I_1 = & \frac{\epsilon_1 \Delta\phi}{l\mu_1 h} \left(\frac{k_B T}{ze}\right)^2 \left[(H_1 \bar{A}_1 - \Psi_{1,w} + \Psi(0^+)) \frac{d\Psi}{dY} \Big|_{Y=0^+} - \bar{A}_1(\Psi_{1,w} - \Psi(0^+)) + f_1 \right] \\ & + \frac{\Delta p h k_B T}{2l\mu_1 z e} \left[H_1(H_1 + \bar{A}_2) \frac{d\Psi}{dY} \Big|_{Y=0^+} + \bar{A}_2(\Psi(0^+) - \Psi_{1,w}) + 2 \int_0^{H_1} (\Psi - \Psi_{1,w}) dY \right]. \end{aligned} \tag{B 10}$$

Here $\bar{A}_2 = A_2/h$, \bar{A}_1 and f_1 are given in (3.16).

Similarly, substituting the velocity (3.10) into (B 7) and using integration by parts, dimensionless variables and (B 4), one can obtain

$$\begin{aligned} I_2 = & \frac{\Delta p h k_B T}{2l\mu_2 z e} \left[\bar{A}_3 \frac{d\Psi}{dY} \Big|_{Y=0^-} + \bar{A}_2(\Psi_{2,w} - \Psi(0^-)) + 2 \int_{-H_2}^0 (\Psi - \Psi_{2,w}) dY \right] \\ & + \frac{\epsilon_1 \Delta\phi}{l\mu_2 h} \left(\frac{k_B T}{ze}\right)^2 \left[\mu_r \bar{A}_4 \frac{d\Psi}{dY} \Big|_{Y=0^-} + \bar{A}_1(\Psi_{2,w} - \Psi(0^-)) + \epsilon_r f_2 \right], \end{aligned} \tag{B 11}$$

where

$$\bar{A}_3 = \frac{\mu_r H_1 H_2 (H_1 + H_2)}{\mu_r H_1 + H_2}, \quad \bar{A}_4 = \frac{H_2 (\Psi_{1,w} - \Psi(0^+)) + \varepsilon_r H_1 (\Psi_{2,w} - \Psi(0^-))}{\mu_r H_1 + H_2}, \quad (\text{B } 12a,b)$$

and f_2 is given in (3.16).

Applying the ion mobility $v_i = ez_i D_i / k_B T$ given by the Nernst–Einstein equation and dimensionless variables, I_3 defined in (B 8) can be rewritten as

$$I_3 = \frac{hze n_\infty}{k_B T} \left[\int_0^{H_1} (D_{+,1} \exp(-\Psi) + D_{-,1} \exp \Psi) dY + b \int_{-H_2}^0 (D_{+,2} \exp(-\Psi) + D_{-,2} \exp \Psi) dY \right]. \quad (\text{B } 13)$$

Finally, after substituting (B 9)–(B 13) into (B 5) and rearranging and simplifying, we derive

$$\begin{aligned} I &= (-\Delta p) \frac{wh\varepsilon_1}{2l\mu_2} \left(\frac{k_B T}{ze} \right) \left[2\mu_r \int_0^{H_1} (\Psi - \Psi_{1,w}) dY + 2\varepsilon_r \int_{-H_2}^0 (\Psi - \Psi_{2,w}) dY \right. \\ &\quad \left. + \bar{A}_1 (H_2^2 - \mu_r H_1^2) \right] + (-\Delta\phi) \frac{w\varepsilon_1^2}{lh\mu_2} \left(\frac{k_B T}{ze} \right)^2 \left[\mu_r f_1 + \varepsilon_r f_2 - \bar{A}_1^2 (H_2 + \mu_r H_1) \right. \\ &\quad \left. + \frac{\mu_2 D_{-,1}}{2\varepsilon_1} \left(\frac{ze}{k_B T} \right)^2 K^2 f_3 \right] + (-\Delta\phi) G_w \\ &\triangleq L_{21}(-\Delta p) + L_{22}(-\Delta\phi). \end{aligned} \quad (\text{B } 14)$$

Appendix C. Energy transfer in nanofluidic channels

The energy transfer in nanofluidic channels can be derived by a combined thermodynamic and fluid mechanics analysis on the system. First, the momentum equation of the system is

$$\rho \frac{d\mathbf{v}}{dt} = -\nabla p + \nabla \cdot \boldsymbol{\tau} + \mathbf{f}, \quad (\text{C } 1)$$

where ρ is the density, \mathbf{v} is the velocity, p is the pressure, $\boldsymbol{\tau}$ is the stress tensor, and $\mathbf{f} = \rho_e \mathbf{E}_s$ is the body force excited by the induced streaming electric field. After forming the dot product of \mathbf{v} with (C 1) and rearranging, one can obtain

$$\rho \frac{d}{dt} \left(\frac{v^2}{2} \right) = -\mathbf{v} \cdot \nabla p + \mathbf{v} \cdot \nabla \cdot \boldsymbol{\tau} + \rho_e \mathbf{v} \cdot \mathbf{E}_s. \quad (\text{C } 2)$$

This is called the mechanical energy equation (Bird, Stewart & Lightfoot 1960). Applying the tensor identity

$$\mathbf{v} \cdot \nabla \cdot \boldsymbol{\tau} = \nabla \cdot (\mathbf{v} \cdot \boldsymbol{\tau}) - \boldsymbol{\tau} : \nabla \mathbf{v}, \quad (\text{C } 3)$$

and integrating the mechanical energy equation over the volume V of the channel, one has

$$\rho \frac{d}{dt} \int_V \left(\frac{v^2}{2} \right) dV = \int_V \mathbf{v} \cdot (-\nabla p) dV + \int_V \nabla \cdot (\mathbf{v} \cdot \boldsymbol{\tau}) dV - \int_V \boldsymbol{\tau} : \nabla \mathbf{v} dV + \int_V \rho_e \mathbf{v} \cdot \mathbf{E}_s dV. \quad (\text{C } 4)$$

The left-hand side represents the rate of change of kinetic energy in V . Here the flow is driven by constant pressure gradient and assumed to be steady and fully developed; thus the kinetic energy of the system is a constant, and the left-hand side of (C4) is identically zero. Applying the divergence theorem to the second term on the right-hand side of (C4) gives

$$\int_V \nabla \cdot (\mathbf{v} \cdot \boldsymbol{\tau}) dV = \int_S (\mathbf{v} \cdot \boldsymbol{\tau}) \cdot \mathbf{n} dS = \int_{S_{wall}} (\mathbf{v} \cdot \boldsymbol{\tau}) \cdot \mathbf{n} dS + \int_{S_{in}} (\mathbf{v} \cdot \boldsymbol{\tau}) \cdot \mathbf{n} dS + \int_{S_{out}} (\mathbf{v} \cdot \boldsymbol{\tau}) \cdot \mathbf{n} dS, \quad (\text{C5})$$

where S is the surface of V , comprising S_{wall} , S_{in} and S_{out} ; and \mathbf{n} is the unit outward normal vector of the surface S . The right-hand side of (C5) represents the viscous shear work on the surface S . Because of the no-slip condition, $\mathbf{v} = 0$ at the channel wall, there is no viscous work on the wall, i.e. the first term on the right-hand side is identically zero. Further, since the velocity profile is the same while the direction of \mathbf{n} is opposite for both the inlet and the outlet, the viscous work at the inlet and outlet surfaces cancel. Therefore, the second term on the right-hand side of (C4) also vanishes.

The third term on the right-hand side of (C4) represents the rate of viscous dissipation in the volume V , which is proportional to the viscosity and evaluated as

$$\boldsymbol{\tau} : \nabla \mathbf{v} \triangleq \mu \Phi. \quad (\text{C6})$$

The viscous dissipation function, Φ , is related to the various spatial derivatives of the velocity for Newtonian fluids. The current density vector in nanochannels can be expressed as

$$\mathbf{j} = \rho_e \mathbf{v} + \sigma \mathbf{E}_s. \quad (\text{C7})$$

The first term on the right-hand side is the contribution from convection; the second is the electro-migration of ions. Here the diffusion of ions is neglected, and σ represents the conductivity of fluids, which generally depends on the location. Applying (C7) to the fourth term on the right-hand side of (C4) gives

$$\int_V \rho_e \mathbf{v} \cdot \mathbf{E}_s dV = \int_V \mathbf{j} \cdot \mathbf{E}_s dV - \int_V \sigma E^2 dV, \quad (\text{C8})$$

where $E = |\mathbf{E}_s|$.

Therefore, evaluation of (C4) at steady state yields simply

$$\int_V \mathbf{v} \cdot (-\nabla p) dV = \int_V \mu \Phi dV + \int_V \sigma E^2 dV + \int_V -\mathbf{j} \cdot \mathbf{E}_s dV. \quad (\text{C9})$$

This is the integral form of the energy equation in the volume V . The left-hand side is the total input power, P_{in} , produced by the pressure work. The first and second terms on the right-hand side are, respectively, viscous dissipation (denoted by P_V) and electrical Joule heating dissipation (denoted by P_E). The third term represents the electrical power that can be output to an external load (denoted by P_{out}) by the nanofluidic system. Note that the direction of the current is opposite to that of the streaming electric field, so the third term is positive. In essence, we ignore the change of internal energy here. Finally, we point out that the energy equation (C9) can apply to various non-Newtonian fluids and any shape of channels.

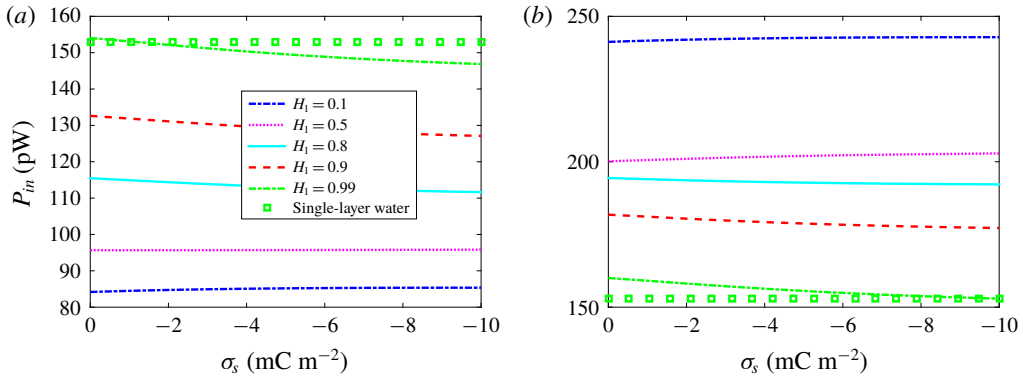


FIGURE 11. (Colour online) The input power P_{in} as a function of interface charge density σ_s and dimensionless thickness H_1 for (a) $\mu_r > 1$ and (b) $\mu_r < 1$. Here the values of the other parameters are the same as in figure 6. The symbol represents the value in single-phase flow, which is a constant independent of the interfacial charges and dimensionless thickness.

For unidirectional and steady two-layer Newtonian fluid flow between parallel plates with viscosities μ_i ($i = 1, 2$), one has

$$P_{in} = \int_V u(y) \left(-\frac{dp}{dx} \right) dV = Q(-\Delta p), \quad (\text{C } 10)$$

$$P_{out} = \int_V j \left(\frac{\Delta\phi}{l} \right) dV = I(\Delta\phi), \quad (\text{C } 11)$$

$$P_V = \int_0^l dx \int_0^w dz \left[\int_0^{h_1} \mu_1 \left(\frac{du}{dy} \right)^2 dx + \int_{-h_2}^0 \mu_2 \left(\frac{du}{dy} \right)^2 dx \right], \quad (\text{C } 12)$$

and $P_E = P_{in} - P_{out} - P_V$. Under the maximum power generation condition, i.e. $\Delta\phi = -\Delta p L_{12} / 2L_{22}$, the input and output powers, and the viscous and electrical Joule heating dissipations can be expressed in terms of the phenomenological coefficients L_{11} , L_{12} and L_{22} as

$$P_{in} = \frac{2 - \alpha}{2} L_{11} \Delta p^2, \quad (\text{C } 13)$$

$$P_{out} = \frac{\alpha}{4} L_{11} \Delta p^2, \quad (\text{C } 14)$$

$$P_E = \frac{\alpha L_{11}}{4L_{22}} L_{22}^{(2)} \Delta p^2, \quad (\text{C } 15)$$

$$P_V = \left[1 - \alpha + \frac{\alpha L_{11}^{(1)}}{4L_{22}} \right] L_{11} \Delta p^2. \quad (\text{C } 16)$$

Here α is the figure of merit, and L_{11} , L_{12} and L_{22} are given in (3.12), (3.13) and (3.15), where L_{22} is divided into two parts as $L_{22} = L_{22}^{(1)} + L_{22}^{(2)}$ according to the contributions from convection and electro-migration of ions, respectively, i.e.

$$L_{22}^{(1)} = \frac{w\varepsilon_1^2}{lh\mu_2} \left(\frac{k_B T}{ze} \right)^2 [\mu_r f_1 + \varepsilon_r f_2 - \bar{A}_1^2 (H_2 + \mu_r H_1)], \quad (\text{C } 17)$$

$$L_{22}^{(2)} = \frac{w\varepsilon_1 D_{-,1}}{2lh} K^2 f_3 + G_w. \quad (\text{C } 18)$$

Note that P_{out}/P_{in} is exactly the efficiency of the system. In figure 11, we show the variations of the input power with the interface charge density σ_s against different values of dimensionless thickness H_1 for the cases of $\mu_r > 1$ and $\mu_r < 1$, respectively. It is observed that P_{in} is almost a constant with respect to σ_s , but depends strongly on H_1 . Furthermore, the effect of H_1 on the input powers is opposite for the viscosity ratios $\mu_r > 1$ and $\mu_r < 1$, which can be attributed to the effect of H_1 on the velocity (see figures 4 and 7a). In addition, the dependences of viscous dissipation and electrical Joule heating dissipation on the interfacial charges and interface location can be found in figures 6 and 9 in both cases.

REFERENCES

- BANDOPADHYAY, A. & CHAKRABORTY, S. 2011 Steric-effect induced alterations in streaming potential and energy transfer efficiency of non-Newtonian fluids in narrow confinements. *Langmuir* **27** (19), 12243–12252.
- BANDOPADHYAY, A. & CHAKRABORTY, S. 2012 Giant augmentations in electro-hydro-dynamic energy conversion efficiencies of nanofluidic devices using viscoelastic fluids. *Appl. Phys. Lett.* **101** (4), 043905.
- BARRY, P. H. & LYNCH, J. W. 1991 Liquid junction potentials and small cell effects in patch-clamp analysis. *J. Membr. Biol.* **121** (2), 101–117.
- BEHRENS, S. H. & GRIER, D. G. 2001 The charge of glass and silica surfaces. *J. Chem. Phys.* **115** (14), 6716–6721.
- BERLI, C. L. A. 2010 Electrokinetic energy conversion in microchannels using polymer solutions. *J. Colloid Interface Sci.* **349** (1), 446–448.
- BIRD, R. B., STEWART, W. E. & LIGHTFOOT, E. N. 1960 *Transport Phenomena*. Wiley.
- BOCQUET, L. & CHARLAIX, E. 2010 Nanofluidics, from bulk to interfaces. *Chem. Soc. Rev.* **39**, 1073–1095.
- BRUNET, E. & AJDARI, A. 2004 Generalized Onsager relations for electrokinetic effects in anisotropic and heterogeneous geometries. *Phys. Rev. E* **69** (1), 16306.
- CHANDA, S., SINHA, S. & DAS, S. 2014 Streaming potential and electroviscous effects in soft nanochannels: towards designing more efficient nanofluidic electrochemomechanical energy converters. *Soft Matt.* **10** (38), 7558–7568.
- CHANG, C. C. & YANG, R. J. 2010 Electrokinetic energy conversion in micrometer-length nanofluidic channels. *Microfluid Nanofluid* **9** (2–3), 225–241.
- CHANG, C. C. & YANG, R. J. 2011 Electrokinetic energy conversion efficiency in ion-selective nanopores. *Appl. Phys. Lett.* **99** (8), 083102.
- CHOI, W. S., SHARMA, A., QIAN, S., LIM, G. & JOO, S. W. 2011 On steady two-fluid electroosmotic flow with full interfacial electrostatics. *J. Colloid Interface Sci.* **357** (2), 521–526.
- CONBOY, J. C. & RICHMOND, G. L. 1997 Examination of the electrochemical interface between two immiscible electrolyte solutions by second harmonic generation. *J. Phys. Chem. B* **101** (6), 983–990.
- DAIGUJI, H., OKA, Y., ADACHI, T. & SHIRONO, K. 2006 Theoretical study on the efficiency of nanofluidic batteries. *Electrochem. Commun.* **8** (11), 1796–1800.
- DAIGUJI, H., YANG, P. & MAJUMDAR, A. 2004a Ion transport in nanofluidic channels. *Nano Lett.* **4** (1), 137–142.
- DAIGUJI, H., YANG, P., SZERI, A. & MAJUMDAR, A. 2004b Electrochemomechanical energy conversion in nanofluidic channels. *Nano Lett.* **4** (12), 2315–2322.
- DAS, S., GUHA, A. & MITRA, S. K. 2013 Exploring new scaling regimes for streaming potential and electroviscous effects in a nanocapillary with overlapping electric double layers. *Anal. Chim. Acta* **804** (804), 159–166.

- DAVIDSON, C. & XUAN, X. 2008a Effects of Stern layer conductance on electrokinetic energy conversion in nanofluidic channels. *Electrophoresis* **29** (5), 1125–1130.
- DAVIDSON, C. & XUAN, X. 2008b Electrokinetic energy conversion in slip nanochannels. *J. Power Sources* **179** (1), 297–300.
- DING, Z., JIAN, Y., WANG, L. & YANG, L. 2017 Analytical investigation of electrokinetic effects of micropolar fluids in nanofluidic channels. *Phys. Fluids* **29** (8), 082008.
- GILLESPIE, D. 2012 High energy conversion efficiency in nanofluidic channels. *Nano Lett.* **12** (3), 1410–1416.
- GOPMANDAL, P. P. & OHSHIMA, H. 2017 Modulation of electroosmotic flow through electrolyte column surrounded by a dielectric oil layer. *Colloid Polym. Sci.* **295** (7), 1141–1151.
- GOSWAMI, P. & CHAKRABORTY, S. 2010 Energy transfer through streaming effects in time-periodic pressure-driven nanochannel flows with interfacial slip. *Langmuir* **26** (1), 581–590.
- GU, Y. & LI, D. 1998 Electric charge on small silicone oil droplets dispersed in ionic surfactant solutions. *Colloids Surf. A* **139** (2), 213–225.
- VAN DER HEYDEN, F. H. J., BONTHUIS, D. J., STEIN, D., MEYER, C. & DEKKER, C. 2006 Electrokinetic energy conversion efficiency in nanofluidic channels. *Nano Lett.* **6** (10), 2232–2237.
- VAN DER HEYDEN, F. H. J., BONTHUIS, D. J., STEIN, D., MEYER, C. & DEKKER, C. 2007 Power generation by pressure-driven transport of ions in nanofluidic channels. *Nano Lett.* **7** (4), 1022–1025.
- VAN DER HEYDEN, F. H. J., STEIN, D. & DEKKER, C. 2005 Streaming currents in a single nanofluidic channel. *Phys. Rev. Lett.* **95** (11), 116104.
- JIAN, Y., LI, F., LIU, Y., CHANG, L., LIU, Q. & YANG, L. 2017 Electrokinetic energy conversion efficiency of viscoelastic fluids in a polyelectrolyte-grafted nanochannel. *Colloids Surf. B* **156**, 405–413.
- JIAN, Y., SU, J., CHANG, L., LIU, Q. & HE, G. 2014 Transient electroosmotic flow of general Maxwell fluids through a slit microchannel. *Z. Angew. Math. Phys.* **65** (3), 435–447.
- LEE, J. S. H., BARBULOVIC-NAD, I., WU, Z., XUAN, X. & LI, D. 2006 Electrokinetic flow in a free surface-guided microchannel. *J. Appl. Phys.* **99** (5), 054905.
- LEE, J. S. H. & LI, D. 2006 Electroosmotic flow at a liquid–air interface. *Microfluid Nanofluid* **2** (4), 361–365.
- LEUNISSEN, M. E., ZWANIKKEN, J., VAN ROIJ, R., CHAIKIN, P. M. & VAN BLAADEREN, A. 2007 Ion partitioning at the oil–water interface as a source of tunable electrostatic effects in emulsions with colloids. *Phys. Chem. Chem. Phys.* **9** (48), 6405–6414.
- LI, D. 2004 *Electrokinetics in Microfluidics*, vol. 2. Elsevier.
- LIU, K., DING, T., MO, X., CHEN, Q., YANG, P., LI, J., XIE, W., ZHOU, Y. & ZHOU, J. 2016 Flexible microfluidics nanogenerator based on the electrokinetic conversion. *Nano Energy* **30**, 684–690.
- MARINOVA, K. G., ALARGOVA, R. G., DENKOV, N. D., VELEV, O. D., PETSEV, D. N., IVANOV, I. B. & BORWANKAR, R. P. 1996 Charging of oil–water interfaces due to spontaneous adsorption of hydroxyl ions. *Langmuir* **12** (8), 2045–2051.
- MASLIYAH, J. H. & BHATTACHARJEE, S. 2006 *Electrokinetic and Colloid Transport Phenomena*. Wiley.
- MEI, L., YEH, L.-H. & QIAN, S. 2017 Buffer anions can enormously enhance the electrokinetic energy conversion in nanofluidics with highly overlapped double layers. *Nano Energy* **32**, 374–381.
- MOVAHED, S., KHANI, S., WEN, J. Z. & LI, D. 2012 Electroosmotic flow in a water column surrounded by an immiscible liquid. *J. Colloid Interface Sci.* **372** (1), 207–211.
- MUNSHI, F. & CHAKRABORTY, S. 2009 Hydroelectrical energy conversion in narrow confinements in the presence of transverse magnetic fields with electrokinetic effects. *Phys. Fluids* **21** (12), 122003.
- NGUYEN, T., XIE, Y., DE VREEDE, L. J., VAN DEN BERG, A. & EIJKEL, J. C. T. 2013 Highly enhanced energy conversion from the streaming current by polymer addition. *Lab on a Chip* **13** (16), 3210–3216.

- OHSHIMA, H., NOMURA, K., KAMAYA, H. & UEDA, I. 1985 Liquid membrane: equilibrium potential distribution across lipid monolayer-coated oil/water interface. *J. Colloid Interface Sci.* **106** (2), 470–478.
- OLTHUIS, W., SCHIPPERS, B., EIJKEL, J. & VAN DEN BERG, A. 2005 Energy from streaming current and potential. *Sensors Actuators B* **111**, 385–389.
- OSTERLE, J. F. 1964 Electrokinetic energy conversion. *Trans. ASME J. Appl. Mech.* **31** (2), 161–164.
- PATWARY, J., CHEN, G. & DAS, S. 2016 Efficient electrochemomechanical energy conversion in nanochannels grafted with polyelectrolyte layers with pH-dependent charge density. *Microfluid. Nanofluid.* **20** (2), 37.
- PENNATHUR, S., EIJKEL, J. C. T. & VAN DEN BERG, A. 2007 Energy conversion in microsystems: Is there a role for micro/nanofluidics? *Lab on a Chip* **7** (10), 1234.
- PRIGOGINE, I. 1968 *An Introduction to Thermodynamics of Irreversible Processes*. Interscience.
- REN, Y. & STEIN, D. 2008 Slip-enhanced electrokinetic energy conversion in nanofluidic channels. *Nanotechnology* **19** (19), 195707.
- SAHA, S., GOPMANDAL, P. P. & OHSHIMA, H. 2017 Steady/unsteady electroosmotic flow through nanochannel filled with electrolyte solution surrounded by an immiscible liquid. *Colloid Polym. Sci.* **295** (12), 2287–2297.
- SCHOCH, R. B., HAN, J. & RENAUD, P. 2008 Transport phenomena in nanofluidics. *Rev. Mod. Phys.* **80** (3), 839.
- SHERWOOD, J. D., XIE, Y., VAN DEN BERG, A. & EIJKEL, J. C. T. 2013 Theoretical aspects of electrical power generation from two-phase flow streaming potentials. *Microfluid. Nanofluid.* **15** (3), 347–359.
- SHIT, G. C., MONDAL, A., SINHA, A. & KUNDU, P. K. 2016 Two-layer electro-osmotic flow and heat transfer in a hydrophobic micro-channel with fluid–solid interfacial slip and zeta potential difference. *Colloids Surf. A* **506**, 535–549.
- SIRIA, A., PONCHARAL, P., BIANCHE, A.-L., FULCRAND, R., BLASE, X., PURCELL, S. T. & BOCQUET, L. 2013 Giant osmotic energy conversion measured in a single transmembrane boron nitride nanotube. *Nature* **494** (7438), 455–458.
- SPARREBOOM, W., VAN DEN BERG, A. & EIJKEL, J. C. T. 2010 Transport in nanofluidic systems: a review of theory and applications. *New J. Phys.* **12** (1), 015004.
- STEIN, D., KRUIHOF, M. & DEKKER, C. 2004 Surface-charge-governed ion transport in nanofluidic channels. *Phys. Rev. Lett.* **93** (3), 035901.
- SU, J., JIAN, Y., CHANG, L. & LI, Q. 2013 Transient electro-osmotic and pressure driven flows of two-layer fluids through a slit microchannel. *Acta Mechanica Sin.* **29** (4), 534–542.
- VOLKOV, A. G., DEAMER, D. W., TANELIAN, D. L. & MARKIN, V. S. 1996 Electrical double layers at the oil/water interface. *Prog. Surf. Sci.* **53** (1), 1–134.
- WANG, M. & KANG, Q. 2010 Electrochemomechanical energy conversion efficiency in silica nanochannels. *Microfluid. Nanofluid.* **9** (2–3), 181–190.
- XIE, Y., SHERWOOD, J. D., SHUI, L., VAN DEN BERG, A. & EIJKEL, J. C. T. 2011 Strong enhancement of streaming current power by application of two phase flow. *Lab on a Chip* **11** (23), 4006.
- XIE, Y., WANG, X., XUE, J., JIN, K., CHEN, L. & WANG, Y. 2008 Electric energy generation in single track-etched nanopores. *Appl. Phys. Lett.* **93** (16), 163116.
- XUAN, X. & LI, D. 2006 Thermodynamic analysis of electrokinetic energy conversion. *J. Power Sources* **156** (2), 677–684.
- YANG, J., LU, F., KOSTIUK, L. W. & KWOK, D. Y. 2003 Electrokinetic microchannel battery by means of electrokinetic and microfluidic phenomena. *J. Micromech. Microengng* **13** (6), 963–970.
- ZHANG, R., WANG, S., YEH, M.-H., PAN, C., LIN, L., YU, R., ZHANG, Y., ZHENG, L., JIAO, Z. & WANG, Z. L. 2015 A streaming potential/current-based microfluidic direct current generator for self-powered nanosystems. *Adv. Mater.* **27** (41), 6482–6487.